HHS Public Access

Author manuscript

Dev Cell. Author manuscript; available in PMC 2023 September 18.

Published in final edited form as:

Dev Cell. 2022 September 26; 57(18): 2181–2203.e9. doi:10.1016/j.devcel.2022.08.009.

Hedgehog signaling activates a mammalian heterochronic gene regulatory network controlling differentiation timing across lineages

Megan Rowton[1], **Carlos Perez-Cervantes**[1], **Suzy Hur**[1], **Jessica Jacobs-Li**[1], **Emery Lu**[1], **Nikita Deng**[1], **Alexander Guzzetta**[1], **Andrew D. Hoffmann**[1], **Matthew Stocker**[1], **Jeffrey D. Steimle**[1], **Sonja Lazarevic**[1], **Sophie Oubaha**[1], **Xinan H. Yang**[1], **Chul Kim**[1], **Shuhan Yu**[1], **Heather Eckart**[1], **Mervenaz Koska**[1], **Erika Hanson**[1], **Sunny S.K. Chan**[2], **Daniel J. Garry**[2], **Michael Kyba**[2], **Anindita Basu**[1], **Kohta Ikegami**[1], **Sebastian Pott**[1], **Ivan P. Moskowitz**[1,*]

[1]Departments of Pediatrics, Pathology, Human Genetics and Genetic Medicine, The University of Chicago, Chicago, Illinois, United States of America

[2]Lillehei Heart Institute, University of Minnesota, Minneapolis, MN 55455, USA; Department of Pediatrics, University of Minnesota, Minneapolis, MN 55455, USA

SUMMARY

Many developmental signaling pathways have been implicated in lineage-specific differentiation, however, mechanisms that explicitly control differentiation timing remain poorly defined in mammals. We report that murine Hedgehog signaling is a heterochronic pathway that determines the timing of progenitor differentiation. Hedgehog activity was necessary to prevent premature differentiation of second heart field cardiac progenitors in mouse embryos and the Hedgehog transcription factor GLI1 was sufficient to delay differentiation of cardiac progenitors *in vitro*. GLI1 directly activated a *de novo* progenitor-specific network *in vitro,* akin to that of second heart field progenitors *in vivo,* which prevented the onset of the cardiac differentiation program. A Hedgehog signaling-dependent active-to-repressive GLI transition functioned as a differentiation timer, restricting the progenitor network to the second heart field. GLI1 expression was associated with progenitor status across germ layers and delayed the differentiation of neural progenitors *in vitro*, suggesting a broad role for Hedgehog signaling as a heterochronic pathway.

INTRODUCTION

Organ development requires stage-specific differentiation (Ebisuya and Briscoe, 2018), however, the molecular basis of differentiation timing control is unknown in most cases.

*Lead contact & corresponding author: imoskowitz@peds.bsd.uchicago.edu.

AUTHOR CONTRIBUTIONS

M.R. designed and performed the experiments and wrote the manuscript. C.P-C. and S.P. also designed experiments. J.J-L, A.G., J.D.S., A.D.H., S.L., S.O., H.E., and M.K performed *in vivo* experiments. S.H., J.J-L., N.D., E.L., M.S., C.K., S.Y., and E.H. performed *in vitro* experiments. M.R., S.P., C.P-C., X.H.Y., S.I. and K.I. performed computational analyses. S.S-K.C. and M.K. generated the GLI1-FTA and GLI3^{R}-FTA mESC lines. D.J.G., S.P. and A.B. designed the experiments. I.P.M. designed the experiments and wrote the manuscript.

COMPETING INTERESTS

The authors report no competing interests.

Explicit genetic control of developmental timing was first described in *C. elegans,* based on mutations that caused premature or delayed progenitor cell state transitions, identifying a class of heterochronic genes (Ambros and Horvitz, 1984). Heterochronic regulators have since been described in other species, including *Drosophila* neuroblast temporal identity factors (Averbukh et al., 2018; Durand and Raff, 2000; Jessell TM, 2000; Pearson and Doe, 2004) and the Delta-Notch oscillatory network controlling vertebrate somitogenesis (Pourquié, 1998). Differentiation timing has been linked to developmental processes, including cell type specification, spatial patterning and proliferation rate (Brown, 2014; Gomez et al., 2008; Harima et al., 2013; Hubaud and Pourquié, 2014; Imayoshi et al., 2013; Kohwi and Doe, 2013; Momen-Roknabadi et al., 2016; Moss, 2007; Otani et al., 2016; Pearson and Doe, 2004; Pourquié, 1998; Weger et al., 2017). However, heterochronic modulators of differentiation timing have proven difficult to identify in mammalian organ development, despite their predicted association with congenital malformations in humans and animal models (Smith, 2003; Wilson, 1988).

Two cardiac progenitor fields, the first heart field (FHF) and the second heart field (SHF), display heterochronic differentiation during mammalian heart development (Kelly et al., 2001). FHF cardiac progenitors (CPs) differentiate early to generate the linear heart tube (HT), reminiscent of the mature heart of invertebrates or lungless vertebrates, including fish. SHF CPs differentiate later, after migrating into the poles of the heart tube, and generate structures required for pulmonary circulation, including the right ventricle, the pulmonary outflow tract and the atrial septum (Kelly, 2012). Although the FHF and SHF are specified toward the cardiomyocyte lineage at a similar developmental timepoint (~E7.25 in the mouse embryo) (Dyer and Kirby, 2009; Lescroart et al., 2014; Meilhac et al., 2004), the molecular mechanism that delays differentiation of the SHF is unknown.

SHF-derived cardiac structures are critical for cardiopulmonary circulation and are often affected in congenital heart disease (CHD), the most common human birth defect (Briggs et al., 2012; Kelly et al., 2014; Neeb et al., 2013). SHF CPs are exposed to a complex intersection of signaling pathways, whose disruption often causes structural heart defects (Bruneau, 2013; Hutson et al., 2010; Jain et al., 2015; Peng et al., 2013; Rankin et al., 2021; Rochais et al., 2009; Xie et al., 2012). For example, CHD-causing mutations are enriched in genes encoding components of the cilium, a cellular organelle essential for the Hedgehog (Hh) signaling pathway (Friedland-Little et al., 2011; Huangfu et al., 2003; Ocbina et al., 2011; Ozanna Burnicka-Turek et al., 2016; Watkins et al., 2019). Disruption of Hh activity in the SHF causes CHD, however the pathophysiological mechanism has not been described (Briggs et al., 2016; Goddeeris et al., 2007; Hoffmann et al., 2009; Xie et al., 2012).

Here, we screened the SHF CM differentiation trajectory for intercellular signaling pathway candidate mediators of heterochronic SHF differentiation control. The Hh signaling pathway was specifically associated with the SHF cardiac progenitor state. We found that Hh signaling was required to prevent cardiac differentiation in the SHF *in vivo*. Consistently, transient activation of the Hh-dependent transcription factor GLI1 delayed cardiomyocyte differentiation from mouse embryonic stem cells *in vitro*. GLI1 induced a novel gene regulatory network (GRN) that globally shifted the epigenetic profile of CPs *in vitro* towards a SHF-like progenitor profile *in vivo* and activated progenitor-specific gene modules.

A transition from active to repressive GLI activity decommissioned progenitor-specific enhancers, restricting their activity to the SHF and permitting cardiac differentiation. GLI1 activity in neural progenitors also caused a heterochronic delay of differentiation. These findings suggest that Hh signaling may function broadly as a heterochronic regulator of progenitor differentiation across germ layers and biological contexts.

RESULTS

Hh signaling is specifically active in the progenitor state *in vivo*

We hypothesized that signal-dependent mechanisms controlled SHF CP differentiation timing. We therefore interrogated signaling pathway activity by single cell transcriptome analysis of the SHF and heart tube (HT) *in vivo*, microdissected from E10.5 mouse embryos (Figure 1A). We defined 19 distinct populations expressing markers of known cell types from all three germ layers by droplet-based single-cell RNA sequencing (Drop-seq) (Figure 1B, Figure S1A–C and Table S1) (Macosko et al., 2015). We then defined four atrial cardiac-associated clusters: two posterior SHF (pSHF) CP populations, an intermediate CP/CM population and an atrial CM population (Figure S1D–H, see Methods). From CPs in the pSHF to functionally differentiated HT CMs in the heart, a single cell transcriptome differentiation continuum was apparent (Figure 1C and Figure S2A). The two CP clusters expressed known pSHF genes *Isl1, Tbx5* and *Arg1* (Figure 1D) (Cai et al., 2003; de Soysa et al., 2019; Xie et al., 2012) and differentially expressed the right-sided marker *D030025E07Rik/Plyrr* lncRNA (Welsh et al., 2015) and left-sided marker *Pitx2* (Chengyu Liu et al., 2002; K. Kitamura, 1999) (Figure S2B–D and Table S1; Figure S2B: two-sided Welch's *t*-test, *D030025E07Rik* $P = 0.0001$, *Pitx2* $P = 0.025$). The intermediate CP/CM cluster was characterized by low expression of genes encoding sarcomere structural components including cardiac troponin T2 (*Tnnt2)* and high expression of the cardiogenic transcription factor (TF) kernel *Tbx5, Gata4* and *Nkx2–5* (Figure 1D and Table S1). The differentiated CM cluster showed high expression of both sarcomere genes and cardiac TFs (Figure 1D and Table S1).

We defined a single cell CP-to-CM differentiation trajectory from the four atrial CM-associated clusters using a set of 24 known CM marker genes (Figure 1E and Figure S2E) (Table S1) (de Soysa et al., 2019). From CP to intermediate to CM stages, we observed a step-wise decrease in cell cycle progression, consistent with a gradient of increasing differentiation (Figure S2F–G). We performed a pairwise differential expression test to confirm expected gene expression differences between the combined CP clusters and the CM cluster. We found 158 CP-enriched genes and 486 CM-enriched ($\log_2$ fold change $\geq$ 0.5, FDR $\leq$ 0.05) (Table S1). CP-enriched genes *Aldh1a2, Arg1* and *Ccdc34* were more highly expressed in cells at the beginning of the pseudotime trajectory and were associated with Gene Ontology (GO) terms consistent with a progenitor state, including cell division and DNA replication (Figure S2H–I). In contrast, CM-enriched genes such as *Tnnc1, Myl4, Nppa* and *Des* were highly expressed in cells at the end of the pseudotime differentiation trajectory and were associated with GO terms indicative of differentiated CMs, such as muscle structure development and actin binding (Figure S2J–K). Furthermore, known CP and CM gene expression patterns aligned with the pseudotime differentiation trajectory

(Figure S2L–M) (Bax et al., 2009; Bertrand et al., 2011; de Soysa et al., 2019; Fujii et al., 2017; Lu et al., 1998; Robb et al., 1998), confirming the differentiating cardiomyocyte lineage.

We investigated the activity of developmental signaling pathways implicated in SHF development across the SHF differentiation trajectory. The Wnt, FGF, Hh, Notch, retinoic acid (RA) and BMP pathways were assessed using expression levels of known target genes as a readout of pathway activity (Bruneau, 2013; Han et al., 2020; Hutson et al., 2010; Jain et al., 2015; Rochais et al., 2009; van Wijk et al., 2007). We observed that Hh, RA and Wnt pathway targets were active in the CP state, FGF and Notch pathway targets became activated in the late CP and intermediate states, and BMP targets became active in the intermediate and CM states, towards the end of the pseudotime trajectory (Figure 1F). We aggregated the expression levels of target genes for each pathway to calculate a general readout of pathway activity. Hh and RA pathways were highly active in the CP state. The BMP pathway was induced prior to the transition between the CP and intermediate states (Figure 2G and Figure S2N), consistent with the known role of BMP signaling in promoting SHF differentiation (Hutson et al., 2010; Tirosh-Finkel et al., 2010; Wang et al., 2010). The Hh pathway demonstrated the most CP-specific activity, based on its steep activity decline between the CP and intermediate states (Figure 1H; two-sided Welch's *t*-test, Hh $P = 4.34E^{-32}$, RA $P = 1.46E^{-17}$, Wnt $P = 0.67$, FGF $P = 2.86E^{-06}$, Notch $P = 0.004$, BMP $P = 2.69E^{-08}$). These data suggested that active Hh signaling was specific to CPs and excluded from differentiating CMs, consistent with a known requirement for Hh signaling in the mammalian SHF for cardiac morphogenesis (Briggs et al., 2016; Goddeeris et al., 2007; Hoffmann et al., 2009; Xie et al., 2012).

Hh signaling prevents premature differentiation and CHD *in vivo*

The specific activity of Hh signaling in CPs suggested a potential role in cardiac differentiation timing control. SHH ligand, expressed in the pulmonary endoderm, activates Hh signaling in the adjacent pSHF mesoderm (Goddeeris et al., 2007; Hoffmann et al., 2009). To investigate the functional role of Hh signaling in the pSHF, we performed bulk RNA-seq analysis of E10.5 Sonic Hedgehog (*Shh)* mutant ($Shh^{-/-}$) and control ($Shh^{+/+}$) micro-dissected pSHFs (Figure 2A). We observed decreased expression of mesenchyme-, mesoderm- and CP-specific genes including *Foxf1*, *Wnt2b*, *Osr1*, and *Snai1* in the $Shh^{-/-}$ mutant pSHF (Figure 2B and Table S2). $Shh^{-/-}$ repressed genes were associated with GO terms such as regionalization, pattern specification, mesenchyme development and heart development (Figure 2C), In contrast, we observed increased expression of CM differentiation genes including *Myl3*, *Tnni3, Kcnj5, Scn5a* and *Nppa* in the $Shh^{-/-}$ mutant pSHF (Figure 2B). $Shh^{-/-}$ activated genes included *Myl3*, *Tnni3, Kcnj5, Scn5a and Hopx,* a promoter of cardiomyocyte differentiation (Jain et al., 2015), and were associated with cardiac differentiation GO terms including muscle cell differentiation, myofibril assembly and the sarcomere (Figure 2D). These data suggested that active Hh signaling promotes CP gene expression and inhibits CM gene expression in the pSHF.

We examined the temporal dynamics of SHF Hedgehog-dependent gene expression to examine the requirement for *Shh* in SHF differentiation control. First, we defined CP- or

CM-enriched gene expression from bulk transcriptional profiling of the wild type pSHF versus HT at E10.0 (Figure 2E, $\log_2$ FC ≥ 0.5, FDR ≤ 0.05, Table S2). We observed that genes repressed in the *Shh*$^{-/-}$ mutant SHF were CP-enriched (Figure 2F; Students *t*-test, both $P = 2e^{-16}$), whereas genes activated in the *Shh*$^{-/-}$ mutant SHF were CM-enriched ($P = 2e^{-16}$). We next assessed the expression dynamics of *Shh*-dependent genes along the CP-to-CM pSHF single-cell pseudotime differentiation trajectory. We observed that genes repressed in the *Shh*$^{-/-}$ mutant SHF were normally CP-expressed in WT embryos, at the beginning of the differentiation trajectory with few exceptions (Figure 2G). In contrast, the majority of genes activated in the *Shh*$^{-/-}$ mutant SHF were normally selectively expressed in the intermediate and CM states in WT embryos (Figure 2H). These findings indicated that *Shh* is required to maintain CP-specific gene expression and suppress CM-specific gene expression in the pSHF, consistent with a role for Hh signaling in the heterochronic control of CP differentiation in the pSHF *in vivo*.

We next examined the spatiotemporal requirement of Hh signaling for pSHF CP differentiation timing *in vivo*. We evaluated myosin heavy chain (MHC) protein expression as a marker of differentiating CMs. MHC expression in wild-type littermate controls was localized to the HT and was excluded from the SHF (Figure 2I). In contrast, MHC expression extended into the SHF in *Shh*$^{-/-}$ mutant embryos at E10.5, including the dorsal mesenchymal protrusion (DMP) (Figure 2I), a structure critical for atrioventricular septation (Snarr et al., 2007). Prior work demonstrated that disruption of Hh singling in *Shh*$^{-/-}$ mice caused Atrioventricular Septal Defects (AVSDs) based on absence of the DMP (Goddeeris et al., 2008; Hoffmann et al., 2014, 2009). These observations link inappropriate differentiation timing of specific SHF progenitors to CHD characterized by the absence of cardiac structures derived from those progenitors in Hh-signaling mutant embryos.

Hh TF GLI1 Delays Differentiation of CPs *in vitro*

We examined the isolated effect of Hh signaling on cardiac differentiation timing in a mouse embryonic stem cell (mESC) directed-differentiation system (Figure S3A) (Kattman et al., 2011). We hypothesized that endogenous Hh signaling would diminish during the CP-to-CM differentiation transition *in vitro*. We confirmed an *in vitro* differentiation trajectory from ES cells to mesoderm to CPs to mESC-CMs, including the activation of known CP markers *Tbx5*, *Nkx2–5* and *Isl1,* at the mESC-CP stage (Days (D) 5–7) by qPCR (Figure S3B). We evaluated endogenous Hh signaling activity during the differentiation time course based on the expression of canonical markers of active Hh signaling, *Gli1*, *Ptch1* and *Hhip*, and the accumulation of activating GLI^{A} TFs (GLI1, GLI2^{A}, GLI3^{A}) at the expense of repressive GLI^{R} TFs (GLI2^{R}, GLI3^{R}) (Dai et al., 1999; Hui and Angers, 2011; Lee et al., 1997; Ruiz i Altaba et al., 2007). We found that endogenous Hh signaling activity was highest in early stages of the differentiation (D0–2), but subsequently decreased after the mesoderm stage. MESCs and mesoderm stage cells expressed *Gli1* and *Ptch1*, markers of active Hh signaling, which became depleted thereafter (Figure S3C). We observed that the relative GLI protein isoform abundance underwent a switch from GLI3^{A} to GLI3^{R} abundance at the CP stage (D4–6) (Figure S3D–F). These results indicated that a transition from active to inactive Hh signaling coincided with mESC-CM differentiation *in vitro*.

We next examined whether maintaining Hh signaling in CPs was sufficient to prevent CP-to-CM differentiation. We specifically hypothesized that maintaining expression of GLI1, an obligate transcriptional activator of Hh signaling, may inhibit CM differentiation. To test this hypothesis, we engineered a transgenic mESC line with doxycycline (dox)-inducible expression of epitope-tagged GLI1 (GLI1-FTA) (Figure 3A) to model GLI1 activation in CPs. To identify the *in vitro* differentiation stage that most accurately represents the SHF, we compared transcriptomes from an mESC-CM differentiation time series (D5–15) with wild type E10.0 pSHF and HT *in vivo* transcriptomes, as well as the publicly-available adult mouse CM transcriptome (Figure 2E) (Akerberg et al., 2019). Principle component analysis demonstrated that the greatest proportion of variation across samples was explained by CM differentiation stage (PC1) (Figure S3G; PC1, 63% of variation, top 10 positive and negative loading genes for PC1 are shown; Table S3). Using correlation and hierarchical clustering analyses, we found that D5–6 mESC-CP *in vitro* transcriptomes most closely resembled the pSHF CP *in vivo* transcriptomes, and that D15 mESC-CM *in vitro* transcriptomes most closely resembled E10.5-E12.5 heart *in vivo* transcriptomes (Figure S3H–I) (Suzuki and Shimodaira, 2006). We therefore chose to transiently activate the expression of the GLI1-FTA transgene at the mESC-CP stage (D5 to D6). We further found that treatment of D5 mESC-CPs with 500ng/ml doxycycline (dox) for 24 hours resulted in activation of Hh target *Gli1* and *Foxf1* to levels similar to those observed in the SHF *in vivo* (Figure 3B, two-sided Students *t*-test, $P = 0.001$; Figure S4A–B), and that Dox washout at D6 resulted in the rapid cessation of *Gli1* transcription (Figure S4E).

We observed that mESC-CM differentiation was transiently blocked by GLI1-FTA overexpression (GLI1 OE) in CPs from D5-D6 (Figure 3C). CM differentiation was significantly reduced at D8, evidenced by decreased relative cTnT-positive area ($P = 0.03$) (Figure 3D–E; two-sided Students *t*-test, $P = 0.07$), decreased number of beating CM foci ($P = 0.01$) (Figure 3F; two-sided Students *t*-test, $P = 0.03$), and a decreased percentage of cells expressing cardiac troponin (cTnT) (Figure S4C; two-sided Students *t*-test $P = 0.18$). However, CM differentiation in GLI1 OE cells rebounded by D12, based on normalization of the percentage of cTnT positive cells ($P = 0.87$), number of beating foci ($P = 0.13$), and relative cTnT+ expression area ($P = 0.07$) between GLI1 OE and control differentiations (Figure 3G–I and Figure S4C; Figure 3H: two-sided Students *t*-test, $P = 0.07$; Figure 3I: two-sided Students *t*-test, $P = 0.13$; Figure S4C: two-sided Students *t*-test $P = 0.87$). GLI1 OE did not cause a significant difference in proliferation rate at D6, D8 or D12, relative to controls (Figure S4D; two-sided Welch's *t*-test, D6 $P = 0.31$, D8 $P = 0.53$, D12 $P = 0.67$). Overall, these observations indicated that transient activation of GLI1 in mESC-derived CPs was sufficient to temporarily delay cardiac differentiation, but did not abrogate CP differentiation potential or enhance CP proliferation.

GLI1 transiently activates a heterochronic regulatory network

We assessed the impact of GLI1 OE on the kinetics of CP-to-CM differentiation gene expression dynamics by RNA-seq at D6, D8 and D12. GLI1 OE for 24 hours from D5–6 caused differential expression of 1,477 genes. However, following dox washout at D6, GLI1-dependent gene expression changes normalized, such that only 74 genes remained differentially expressed by D12 (Figure 3J). Rapid normalization of CP (*Gli1, Foxf1 and*

Bra) and CM (*Tnnt2, Myh6* and *Hand2*) gene expression was observed by qPCR (Figure S4E–F; Kruskal-Wallis rank sum test for D6, D8 and D12 samples: D6 $P < 2e^{-16}$, D8 $P < 2e^{-16}$, D12 $P < 2e^{-16}$, post-hoc *t*-tests, all days $P = 2e^{-16}$, D12 repressed vs all $P = 2e^{-16}$, D12 repressed vs activated $P = 2e^{-16}$, D12 all vs activated $P = 5e^{-9}$; Table S4), consistent with the normalized CM phenotype by D12. Supporting this observation, correlation scores of GLI1 OE and control replicate transcriptomes clustered by treatment at D6, but not at D12 (Figure S4G).

Activation of GLI1 in mESC-CPs from D5–6 resulted in increased expression of known SHF Hh signaling targets and CP-specific genes *Gli1, Ptch1, Foxd1, Foxf2,* and *Osr1* (Hoffmann et al., 2014), and decreased expression of CM differentiation genes, including *Tnnt2*, *Myh6* and *Hand2* (Figure 3L). GLI1 OE activated genes were associated with developmental GO terms including cardiovascular system development, mesenchymal cell differentiation and receptor-ligand activity (Figure 3M). GLI1 OE repressed genes, on the other hand, were associated with GO terms including muscle structure development, muscle contraction and cardiomyocyte differentiation (Figure 3N). Furthermore, PC1-positive loading genes identified in the differentiation time series PCA (Figure S3G), which included cardiomyocyte markers *Myh6, Kcnj5, Scn5a* and *Erbb4*, were repressed upon GLI1 OE at D6 (Figure 3O; Exact test, *Myh6* FDR = $6.2E^{-5}$, *Kcnj5* FDR = $8.98E^{-14}$, *Scn5a* FDR = $7.5E^{-5}$, *Erbb4* FDR = $9.1E^{-4}$; Figure S4H; Students *t*-test, $P = 0.0002$).

We next compared the genes dysregulated by GLI1 OE *in vitro* to wild type SHF- and HT-specific gene expression during cardiomyocyte differentiation *in vivo* at E10.5 (Figure 3P). GLI1 induction *in vitro* caused global activation of pSHF-specific genes and repression of HT-specific genes (Figure 3Q; Student's *t*-test, activated vs all expressed genes $P = 7.16e^{-20}$, repressed vs all expressed genes $P = 1.49e^{-57}$). We examined GLI1-dependent genes within the high-resolution Drop-seq pseudotime SHF cardiac differentiation trajectory. GLI1 *in vitro*-activated genes were sorted into four clusters along the differentiation trajectory, with the majority expressed in two CP-enriched clusters (Figure S4I, clusters A and B). GO terms associated with these genes included Hh-dependent processes such as ureteric bud development, heart development, and basal cell carcinoma. In contrast, genes repressed by GLI1 *in vitro* sorted into two clusters enriched for CM-expressed (cluster A) and intermediate state-expressed (cluster B) genes, with corresponding GO terms related to heart development, heart contraction, and heart conduction (Figure S4J), and included both the drivers (*Gata4, Tbx3*) and functional products (*Ryr2, Kcnj5*) of cardiac differentiation. Taken together, these results support a heterochronic model in which transient GLI1 OE is sufficient to delay the onset of the CM differentiation gene expression program and promote the maintenance of a CP expression profile reminiscent of the embryonic pSHF, without promoting alternative cell fates.

GLI1 directly activates CP genes via distal enhancers

To elucidate the direct targets of GLI1-mediated heterochronic regulation, we identified GLI1 binding locations in conjunction with histone modifications in mESC-CPs genome-wide (Figure 4A). GLI1 chromatin affinity purification followed by sequencing (ChAP-seq) in mESC-CPs at D6 after dox-induction of GLI1-FTA at D5 (Figure 4B) identified

a consensus set of 2,876 binding events between 2 biological replicates (Figure S5A). The GLI TF binding motif was the most enriched motif at GLI1 bound regions (Figure S5B). Consistent with GLI localization patterns in other tissues, GLI1 bound to previously identified enhancers at the known GLI target gene *Ptch1* (Figure S5C) and was primarily localized at intergenic (46%) or intronic (41%) regulatory elements compared to gene promoters (5%) (Figure 4C) (Peterson et al., 2012; Vokes et al., 2008, 2007).

We assessed the impact of GLI1 binding on the active enhancer landscape of CPs by assessing enrichment of the H3K27ac histone modification, a hallmark of active enhancers (Creyghton et al., 2010), using chromatin immunoprecipitation (ChIP-seq). We found that GLI1 OE increased the number of active enhancers by ~16,000 globally (Figure S5D) and that GLI1 binding sites showed dramatically increased H3K27ac levels in GLI1 OE CPs relative to control CPs (Figure 4D–E; Wilcoxon signed-rank test, $P < 2e^{-16}$). In fact, the vast majority (1,979 / 2,437 (81%) of GLI1 bound regions gained H3K27ac in GLI1 OE CPs (Figure 4F), including highly activated previously identified enhancers near *Ptch1* (Figure S5E) (Vokes et al., 2008, 2007). We defined putative direct GLI1 target genes as those with activated expression upon GLI1 OE and within 200kb of at least one GLI1-activated enhancer; which encompassed the majority (71%) of GLI1-activated genes (Figure S5F). Putative direct GLI1 targets demonstrated larger increases in gene expression than indirect target genes (Figure S5G; two-sided Student's *t*-test, $P = 0.04$) and direct target transcriptional start sites (TSSs) demonstrated increased enrichment of H3K27ac upon GLI1 OE (Figure S5H; two-sided Student's *t*-test, $P = 1.99e^{-13}$). Together, these results deliver the GLI1 gene regulatory network (GRN) in CPs, defined by the set of 599 GLI1-bound and activated enhancers (GLI1 GRN enhancers) and their 430 putative direct target genes (GLI1 GRN genes) in CPs (Table S5).

We identified GLI1 GRN gene modules as candidate mediators of the heterochronic activity of GLI1. We assessed whether GLI1 may control mESC-CP heterochrony by direct regulation of cell cycle regulators, which are known GLI1 direct targets in some contexts (Agathocleous et al., 2007). We examined the genomic regions around three direct GLI1 target genes from other cell types, *Ccnd1* (Hasenpusch-Theil et al., 2018), *Cdk6* (Hu et al., 2006) and *Mync* (Hu et al., 2006; Singh et al., 2018). Only the *Ccnd1* locus contained GLI1 GRN enhancers (Figure S5I, grey boxes); none of these genes contained a GLI1 activated enhancer near their respective TSSs, and in fact, each showed slightly decreased H3K27ac enrichment upon GLI1 OE. We conclude that direct control of cell cycle regulatory machinery activated by GLI1 in other contexts is unlikely to contribute to GLI1-dependent heterochrony in mESC-CPs. In contrast, we observed a concentration of GLI1 GRN enhancers near genes associated with two functional categories: developmental regulators and genes affiliated with cell adhesion or migration. GLI1 GRN developmental regulators included transcription factors and signaling components, such as *Foxf2* (Bademci et al., 2019; Hoffmann et al., 2014; Nik et al., 2016), *Sox11* (Bergsland et al., 2006; Hoshiba et al., 2016; Paul et al., 2014) and *Notch2* (Tchorz et al., 2012; Wang et al., 2012; Yang et al., 2012), and were mostly expressed in the CP stage of the Drop-seq pseudotime differentiation trajectory (Figure 4G), suggesting that they represent GLI1 targets in the SHF. GLI1 GRN adhesion / migration regulators were also expressed in the CP or intermediate differentiation stages (Figure 4H), and many were associated with

adhesion signaling or axon guidance GO terms. GLI1 bound and activated multiple GLI1 GRN enhancers near developmental regulators and adhesion/migration genes, including *Ncor2* (Jepsen et al., 2000; Wei et al., 2014), *Smad3* (Datto et al., 1999; Tomic et al., 2004), *Sema3e* (Gitler et al., 2004; Gu et al., 2005; Sakurai et al., 2010) and *Snai1* (Gentile et al., 2021; Li et al., 2019; Sun et al., 2018) (Figure 4I–J, grey boxes), suggesting that GLI1 many engage multiple distal enhancers for the induction of these target genes. These results demonstrate that GLI1 functions to directly activate multiple CP stage-specific gene expression modules, potentially integrating several facets of progenitor cell identity.

GLI1 activates a heterochronic pSHF-like GRN *de novo*

We examined the impact of GLI1 OE on chromatin accessibility at GLI1 GRN enhancers by performing an assay for transposase-accessible chromatin (ATAC-seq) (Buenrostro et al., 2013) on D7 GLI1 OE and control cells (Figure 5A). We observed increased chromatin accessibility across GLI1 GRN enhancers in GLI1 OE CPs relative to control CPs at D7 (Figure 5B–C; two-sided Student's *t*-test, $P < 2e^{-16}$), and GLI1 OE led to a global increase in the number of accessible regions (Figure S5J; 59,212 vs 64,173 accessible regions in control vs GLI1 OE samples). Increased chromatin accessibility was observed near known GLI target genes, including *Ptch1* (Figure S5K). GLI1-bound regions showed larger increases in both H3K27ac enrichment and chromatin accessibility than unbound regions in response to GLI1 OE (Figure 5D; ATAC-seq two-sided Welch's t-test, $P < 2e^{-16}$; ChIP-seq two-sided Welch's t-test, $P < 2e^{-16}$). Together, these results suggested that GLI1 may activate a heterochronic enhancer network through the induction of both histone-modifying and chromatin-remodeling activities at GLI1 GRN enhancers in mESC-CPs.

We asked whether GLI1 increased H3K27ac enrichment and chromatin accessibility at an extant CP enhancer network or if it instead superimposed a *de novo* GLI1-dependent network onto CPs. To differentiate these possibilities, we decoupled the effects of differentiation timing from the effects of GLI1 OE by defining the epigenomic ground state of CPs at D5, prior to the initiation of GLI1 OE (Figure 5A). We observed that almost all GLI1 GRN enhancers (533/599, (89%)) were inaccessible prior to GLI1 OE at D5 (Figure 5E). GLI1-mediated H3K27ac deposition at D6 was significantly higher at GLI1 GRN enhancers that were inaccessible at D5 than at those that were previously accessible at D5 (Figure S5L; Wilcoxon signed-rank test, $P = 2.45e^{-9}$). We next intersected D5 accessible chromatin regions with D7 accessible regions in control versus GLI1 OE samples to characterize the stage- versus treatment-specificity of GLI1 GRN enhancers. We found that most GLI1 GRN enhancers were enriched in regions that were accessible only in D7 GLI1 OE cells (274 newly accessible enhancers, enrichment odds ratio 4.7), however, some regions were accessible in both D5 and D7 GLI1 OE cells but not in D7 control cells (26 previously accessible enhancers, enrichment odds ratio 2.4) (Figure 5F; one-sided Fishers exact test, D7 GLI1 OE $P = 6e^{-55}$, D5:D7 GLI1 OE $P = 1e^{-4}$). These results suggest that GLI1 primarily opens and activates a *de novo* set of Hh signal-dependent enhancers, but also maintains accessibility of a small number of previously open enhancers at GLI1 GRN genes in mESC-CPs. Interestingly, several of the GLI1 GRN enhancers with D5 accessibility prior to GLI1 OE were located at Hedgehog signaling component genes themselves, including *Ptch1*, which had 2 D5 accessible enhancers and 13 *de novo* accessible enhancers (Figure

5G). Together, these observations suggest that GLI1 predominately binds directly to closed chromatin near its target genes and promotes the epigenetic remodeling and *de novo* activation of a signal-dependent GRN in mESC-CPs to maintain the progenitor state.

We hypothesized that the *de novo* GLI1 GRN established a specialized, paused-CP epigenomic state reminiscent of the SHF *in vivo*. We therefore compared E10.0 pSHF chromatin accessibility *in vivo* (Figure 5H) with D7 CP accessibility in the presence and absence of GLI1 OE *in vitro*. We observed a much stronger correlation between the pSHF and D7 GLI1 OE mESC-CPs at GLI1 GRN enhancers than between the pSHF and control mESC-CPs (Figure 5I, $R^2 = 0.65$ vs $R^2 = 0.40$, Fisher's *Z*-transformation, $P < 2e^{-16}$). GLI1 activity was therefore sufficient to partially transform the epigenetic landscape of CPs *in vitro* towards that of the pSHF *in vivo*. This epigenetic transformation was especially apparent at regions near SHF-expressed GLI1 GRN genes, including a region 76kb upstream of *Foxf1* (Figure 5J, grey boxes).

GLI TFs comprise a heterochronic transcriptional timer in the SHF

Given that the GLI1 GRN maintained the progenitor status of mESC-CPs, we predicted that GLI1 GRN enhancers would show progenitor-specific activity that was decommissioned during cardiac differentiation *in vivo*. We compared the spatiotemporal accessibility of GLI1 GRN enhancers in CPs, differentiating CMs, and terminally differentiated CMs *in vivo* (Figure 6A). We defined a union set of 105,618 regions accessible in the E10.0 pSHF (Figure 5H), E10.0 HT (Figure 6A) or the adult mouse heart (Liu et al., 2019) and filtered GLI1 GRN enhancers to exclude sites that were inaccessible *in vivo* (Figure S6A; 402/599 inaccessible enhancers). We found that *in vivo*-accessible GLI1 GRN enhancers demonstrated robust accessibility in the pSHF, diminished accessibility in the embryonic HT, and little-to-no accessibility in the mature heart (Figure 6B–C; Kruskal-Wallis test, $P < 2e^{-16}$; post-hoc *t*-tests, all $P < 2e^{-16}$), decreasing in step-wise fashion during differentiation. The gradual loss of accessibility of GLI1 GRN enhancers *in vivo* suggested that it was it unlikely that chromatin condensation was responsible for decommissioning the GLI1 GRN as CMs initiate differentiation.

We hypothesized that a Hh-dependent GLI^A-to-GLI^R TF transition may instead function as a molecular timer at GLI1 GRN enhancers to regulate the spatiotemporal activity of the GLI1 GRN. We examined the GLI^A / GLI^R ratio in CPs and CMs *in vivo* (Figure 6A). Western blot analysis on microdissected embryonic pSHF and HT revealed the expression of GLI1 only in the pSHF, not in the HT (Figure 6D). Quantification of the overall abundance of GLI^A and GLI^R in the pSHF and HT demonstrated a dramatic decrease in the proportion of GLI^A TFs between the pSHF and the HT (Figure 6E). The difference in the localizations of GLI^A and GLI^R in the embryo suggested that CPs encounter a GLI^A-to-GLI^R abundance transition as they move away from the pulmonary endoderm source of SHH ligand and towards the heart tube to differentiate into CMs.

We predicted that repressive GLI TFs, such as $GLI3^R$, would bind to the same enhancers as GLI1 and abrogate their activity as CPs initiated differentiation (Figure 6F). We engineered a transgenic mESC line with dox-inducible expression of epitope-tagged $GLI3^R$ ($GLI3^R$-FTA) and used it to perform $GLI3^R$ ChAP-seq in mESC-CPs at D6 (Figure 6G). We

observed robust GLI3^R enrichment at GLI1 GRN enhancers (Figure 6H). GLI3^R was bound within 200kb of 63% (269/430) of GLI1 GRN genes (Figure 6I), suggesting that many GLI1 GRN enhancers may be decommissioned by GLI3^R. We previously identified an enhancer near the GLI1 GRN gene *Foxf1* (Fox enhancer) that was bound and activated by GLI1 and the cardiogenic TF TBX5 and demonstrated pSHF-restricted activity *in vivo* (Hoffmann et al., 2014). The chromatin at this enhancer was accessible in both the embryonic pSHF and HT states, raising the possibility that enhancer activity may be dictated by GLI isoform abundance, activated by GLI^A in the pSHF and silenced by GLI3^R in the HT (Figure 6J). Chromatin at this enhancer became *de novo* accessible and H3K27ac-enriched upon GLI1 OE and was bound by GLI3^R in GLI3^R OE CPs *in vitro*. We assessed the quantitative effects of GLI1, GLI3^R, and TBX5 on Fox enhancer activity in a luciferase reporter assay. Co-transfection with TBX5 alone activated the Fox enhancer to a modest degree (Figure 6K). Co-transfection of GLI1 with TBX5 dramatically enhanced Fox enhancer activity (two-sided Student's *t*-test, $P = 0.04$), whereas co-transfection of GLI3^R with TBX5 silenced enhancer activity (two-sided Students *t*-test, $P = 0.02$). Mutation of GLI binding sites (GBSs) within the enhancer abrogated, but did not completely suppress, cooperative activation, suggesting that GLI1/3^R and TBX5 may physically interact to regulate gene expression. These results indicated that the GLI^A / GLI^R ratio was a dominant predictor of Fox enhancer activity that may represent a functional high-to-low GLI activity transition restricting GLI1 GRN activity to CPs.

We predicted that the GLI^A-to-GLI^R transition functionally determined the SHF-specific domain of Fox enhancer activity *in vivo*. We rendered the enhancer impervious to the GLI^A / GLI^R molecular switch by mutating all three GBSs. Whereas the wild-type enhancer drove reporter expression selectively in the SHF *in vivo,* the GBS mutant enhancer consistently drove reporter expression in both the SHF and ectopically in the HT in transient transgenic embryos at E10.0 (Figure 6L, Figure S6B–C). This observation suggests that while non GLI TFs (such as TBX5) were sufficient to drive activity of the GBS mutant enhancer in the SHF, decommissioning of the enhancer in differentiating CMs required GLI^R activity. These data support a model in which the spatial distribution of GLI^A / GLI^R TFs in the pSHF and HT comprises a dominant progenitor-on / cardiomyocyte-off molecular timing mechanism to activate and restrict the activity of the GLI1 GRN to CPs and only permit CM differentiation in time and space after CPs escape active Hh signaling in the SHF and enter the HT.

This model predicted that prematurely overriding GLI^A activity with GLI^R in SHF CPs would cause premature SHF differentiation, which we tested by conditionally upregulating GLI3^R in the pSHF. We employed a pSHF-specific, tamoxifen-inducible Cre recombinase line (*Osr1*$^{eGFPCre\text{-}ERT2/+}$) to overexpress GLI3^R (from *ROSA26*$^{Gli3R\text{-}Flag/+}$) (Mugford et al., 2008; Vokes et al., 2008). Embryos with GLI3^R overexpression (*Osr1*$^{eGFPCre\text{-}ERT2/+}$; *ROSA26*$^{Gli3R\text{-}Flag/+}$ embryos; GLI3^R OE) demonstrated precocious CM differentiation in the DMP, a pSHF region otherwise occupied by undifferentiated, mesenchymal progenitor cells in wild-type controls, as assessed by MYL7 expression (Figure 6M, yellow arrowheads) and MF20 staining (Figure S6D). Cells in the DMP normally migrate into the heart to form the atrial portion of the atrioventricular septum (AVS). However, in GLI3^R OE mutants, this structure was hypoplastic or missing entirely, causing atrioventricular

septal defects at E14.5 (Figure 6N). Together, these findings indicated that GLI^A TFs function as a heterochronic timing mechanism in the SHF *in vivo*, required to activate and maintain a signal-dependent, progenitor-specific GRN and inhibit premature onset of the cardiomyocyte differentiation program, thereby preventing CHD.

GLI1 Delays Differentiation of mESC-derived Neural Progenitors

The widespread deployment of Hh signaling during organ development suggested that Hh signaling may function as a heterochronic differentiation timer in other developmental contexts. We first queried whether Hh signaling activity was restricted to the progenitor state in diverse cell types during development. Using *Gli1* expression as a marker of active Hh signaling (Lee et al., 1997), we assessed Hh signaling activity dynamics during the differentiation of mouse and human tissues representing all three developmental germ layers using publicly available RNA-seq datasets (Bernstein et al., 2010; ENCODE Consortium, 2012; Gascard et al., 2015; Herzog et al., 2017; Lister et al., 2009; Weintraub et al., 2017; Zhang et al., 2017) (Table S6). As cellular differentiation progressed from the stem cell stage to the progenitor stage to terminally differentiated cell types, we observed a consistent decrease of *Gli1* expression ranking in ectoderm, mesoderm and endoderm-derived tissues from both mouse and human (Figure 7A; ANOVA followed by post-hoc *t*-tests for *Gli1* rank in ectoderm: $P = 3.89e^{-5}$; mesoderm: $P = 0.01$; endoderm: $P = 5.54e^{-5}$). *Gapdh* expression ranking remained consistently expressed during the course of cellular differentiation (ANOVA followed by post-hoc *t*-tests for *Gapdh* rank in ectoderm: $P = 0.07$; mesoderm: $P = 0.15$; endoderm: $P = 0.59$). We next identified all genes differentially expressed between the stem or progenitor stages and the differentiated cell stage for each germ layer. *Gli1* was differentially expressed in all mouse and human germ layer differentiation time series, showing higher expression in the stem cell stage than the differentiated cell stage (Figure S7A; ANOVA for *Gli1* rank in three mouse groups: $P\text{-value} = 1.15e^{-4}$, post-hoc Tukey Test: stem vs progenitor $P\text{-value} = 0.14$, stem vs differentiated $P\text{-value} = 1.56e^{-4}$, progenitor vs differentiated $P\text{-value} = 1.39e^{-3}$; ANOVA for *Gapdh* rank in three mouse groups: $P\text{-value} = 0.03$; ANOVA for *GLI1* rank in three human groups: $P\text{-value} = 1.25e^{-6}$; post-hoc Tukey Test: stem vs progenitor $P\text{-value} = 1.70e^{-4}$, stem vs differentiated $P\text{-value} = 7.0e^{-7}$, progenitor vs differentiated $P\text{-value} = 0.12$. ANOVA for *GAPDH* rank in three human groups: $P\text{-value} = 0.22$.). GO term analysis of genes more highly expressed in the progenitor state than the differentiated state identified the Hh-related terms “Hedgehog signaling pathway” and “Basal cell carcinoma” as well as expected progenitor-associated terms such as “DNA replication” and “cell cycle,” and (Figure 7B). These results suggested that Hh signaling activity was generally higher in stem and progenitor cell states than in differentiated cell states across cell types in both human and mouse, consistent with the possibility that Hh signaling may be required to maintain progenitor status and prevent differentiation as a heterochronic regulator across tissues.

We considered neuronal development specifically, as Hh signaling has a well-documented role in neural specification (Belgacem et al., 2016; Briscoe et al., 2000; Dessaud et al., 2008; Ericson et al., 1996; Fuccillo et al., 2006) and we reasoned that Hh/GLI1 might also exert a heterochronic effect in neuronal progenitors. We performed a directed differentiation of GLI1-FTA mESCs into the neuronal lineage from neuro-ectodermal progenitors (D2–4), to

neural progenitors/neurospheres (mESC-NPs, D4–6), to immature neurons with an axonal network (D6–8) (Kutejova et al., 2016; Sasai et al., 2014) (Figure S7B). Dynamic marker gene expression characteristic of neuronal progenitors (*Sox1, Nestin*) and differentiating neurons (*Tubb3*) confirmed the differentiation staging (Figure S7C). While endogenous Hh signaling, as reflected by *Gli1, Ptch1* and *Hhip* expression, appeared active throughout the course of neural differentiation, it became reduced during the mESC-NP stage (Figure S7D), suggesting that the reduction of Hh signaling may permit the transition from neuronal progenitors to immature neurons.

We found that transient GLI1 OE in neuronal progenitors was sufficient to delay the onset of neuronal differentiation. Treatment of neural progenitors from D3-D5 with 500ng/ml dox for 48 hours resulted in robust *Gli1* expression (Figure 7C–D, Figure S7E; two-sided Students *t*-test, $P = 0.001$). In control cells, axons marked by expression of the pan-neuronal microtubule marker Tubulin β-3 (*Tubb3*/TUJ1) spanned two or more neurospheres by D5 (Figure 7E–G). In contrast, in GLI1 OE mESCs, axon emergence (two-sided Students *t*-test, $P = 0.0024$) and Tubulin β-3 expression (two-sided Students *t*-test, $P = 0.0018$) were significantly reduced at D5 (Figure 7E–G), although the overall number and size of neurospheres remained unaffected (Figure S7F). At D10, five days after dox washout, a robust axon network had formed in both GLI OE and control cells and TUJ1-expression was statistically indistinguishable between the two (Figure 7H–I; two-sided Students *t*-test, $P = 0.1562$). These observations suggested that transient GLI1 OE delayed, but did not permanently prevent, neuronal differentiation.

The delayed differentiation of neuronal progenitors was reflected by global analysis of gene expression. GLI1 OE (D3–5) caused altered expression of 523 genes in neuronal progenitors compared to control progenitors at D5, including activation of known GLI^A targets in the neural tube, such as *FoxA2* and *Nkx2–2* (Kutejova et al., 2016; Peterson et al., 2012), and neural progenitor markers, such as *Neurog3* (Carcagno et al., 2014) and *Nkx2–9* (Jarrar et al., 2015; Pabst et al., 2003) (Figure 7K–L and Table S7; Exact test, *Neurog3* FDR = $1.6E^{-6}$, *Nkx2–9* FDR = $1.3E^{-170}$, *Sox5* FDR = $5.3E^{-3}$). We also observed repression of markers of neuronal differentiation, including *Nefm* (Carden et al., 1987), *Cntn2* (Suter et al., 2020) and *Ntrk2* (Baydyuk et al., 2011; Marler et al., 2008), and neurogenic transcription factors, such as *Lhx1* (Bedont et al., 2014; Inoue et al., 2013; Zhao et al., 2007) and *Pou4f1* (Lanier et al., 2009; McEvilly et al., 1996; Xiang et al., 1996) (Figure 7K–L and Table S7; Exact test, *Nefm* FDR = $5.1E^{-34}$, *Cntn2* FDR = $6.6E^{-5}$, *Ntrk2* FDR = $2.95E^{-16}$, *Lhx1* FDR = $1.3E^{-5}$ *Pou4f1* FDR = $1.1E^{-5}$ *Pax3* FDR = $9.8E^{-3}$). By D10, however, gene expression alterations in GLI1 OE mESC-NPs had almost entirely normalized, similar to our observations in mESC-CPs. Consistent with phenotypic recovery of axonal differentiation, only 13 genes remained dysregulated at D10 (Figure 7M–N, Figure S7G–H and Table S7; 7N boxplots: Kruskal-Wallis test, $P < 2e^{-16}$; post-hoc *t*-tests, repressed vs all $P = 6.7e^{-15}$, repressed vs activated $P = 4.8e^{-15}$, all vs activated $P = 4.3e^{-5}$; Figure S7H: two-sided Students *t*-test, *Tubb3* D4–6 $P < 0.05$). Overall, these results suggest that Hh signaling activates transient, progenitor stage-specific heterochronic transcriptional programs to temporarily pause differentiation across somatic cell lineages.

DISCUSSION

We report that Hh signaling functions as a heterochronic pathway to control differentiation timing, apparently without altering cell fate potential, in multiple developmental contexts. A direct role for Hh signaling in heterochronic differentiation control may underlie many functions ascribed to Hh signaling in diverse cellular contexts. Hh signaling has been implicated in organ-specific progenitor functions, including cell migration, proliferation, and mammalian organ morphogenesis (Agathocleous et al., 2007; Briscoe and Thérond, 2013; Ingham and Placzek, 2006; Jiang and Hui, 2008; Kaldis and Richardson, 2012; Lee et al., 2016; Liu and Ngan, 2014). Global disruption of Hh signaling or GLI transcription factors (TFs) cause pleiotropic developmental syndromes including VACTERL syndrome, Gorlin Syndrome, holoprosencephaly and Greig cephalopolysyndactyly syndrome (Friedland-Little et al., 2011; Hui and Angers, 2011; McMahon et al., 2003; Ngan et al., 2012; Nieuwenhuis and Hui, 2005). Further, Hh signaling has been implicated in the maintenance of adult stem cells required for organ homeostasis (Beachy et al., 2004a; Petrova and Joyner, 2014; Roy and Ingham, 2002). A heterochronic role maintaining progenitor status is also consistent with the described role for Hh signaling in injury-induced regeneration of the heart (Kawagishi et al., 2018; Singh et al., 2018; Wang et al., 2015), bladder (Shin et al., 2011), prostate (Karhadkar et al., 2004), bone (Miyaji et al., 2003), tooth (Zhao et al., 2014), liver (Ochoa et al., 2010), and lung (Peng et al., 2015; Watkins et al., 2003). Whereas controlled Hh signaling in adult stem cells has been associated with organ homeostasis and regeneration, uncontrolled Hh activation promotes cancer, including medulloblastoma, basal cell carcinoma, and rhabdomyosarcoma (Hooper and Scott, 2005; Jiang and Hui, 2008; Ng and Curran, 2011; Taipale and Beachy, 2001; Wicking et al., 1999). Hh signaling in cancer has been hypothesized to function through promotion of cancer stem cells (Beachy et al., 2004b; Ruiz i Altaba et al., 2002; Teglund and Toftgård, 2010). However, in most of these contexts, the transcriptional networks activated by the GLI TFs remain to be elucidated. Therefore, whether previously observed Hh-dependent phenomenology reflects heterochronic control of progenitor status or direct molecular control of other developmental events remains unclear.

Integrating the heterochronic role of Hh signaling in differentiation timing control with the additional roles of Hh signaling may bring insight to complex organogenesis. In addition to direct GLI1-dependent control of developmental transcription factors and signaling components, we identified GLI1 GRN enhancers near cell adhesion and migration genes. Coordinated GLI1-dependent control of CP cell motility and differentiation status is a logical possibility in heart development, given the requirement that Hh-receiving progenitors migrate from the Hh-receiving SHF into the heart tube to escape Hh signal, undergo a GLI^A-to-GLI^R switch, and initiate differentiation. Hh-dependent GRNs directly affect cell fate determination or patterning in some developmental contexts, including the limb and neural tube (Lei et al., 2006; Oosterveen et al., 2012; Peterson et al., 2012; Sasaki et al., 1997; Vokes et al., 2008, 2007). Description of coincident, distinct Hh-dependent GRNs that control patterning and differentiation timing suggests that the transcriptional basis of these two developmental phenomena may be linked. Sub-domains of the neural tube and limb with the highest Hh activity sustain high expression of progenitor-specific genes relative to

Hh-deficient domains (Delile et al., 2019; Reinhardt et al., 2019). As in the pSHF, GLI^A TFs in the neural tube drive expression of repressive TFs that prevent the acquisition of gene expression for alternative cell fates (Kutejova et al., 2016). Interestingly, Hh-dependent transcriptional repression of neural differentiation effector genes is also observed in the neural tube, suggesting a possible coincident heterochronic role (Balaskas et al., 2012; Kutejova et al., 2016). Dissection of the heterochronic function of Hh signaling from alternate Hh-dependent developmental mechanisms will require further investigation of the overlapping and distinct Hh/GLI-dependent GRNs in each context.

Signal-dependent transcription factors often bind accessible *cis*-regulatory elements previously occupied by lineage-determining transcription factors (Carroll et al., 2005; Heinz et al., 2010; John et al., 2011; Magnani et al., 2011; Mukherjee et al., 2020; Mullen et al., 2011; Tan et al., 2011; Trompouki et al., 2011). In contrast, we found that GLI1 primarily bound to genomic locations that were inaccessible at the time of GLI1 deployment in mESC-CPs. The binding of GLI1 subsequently caused increased accessibility and H3K27ac deposition, establishing a *de novo* GRN in Hh-naïve cardiac progenitors. Consistent with these observations, GLI TFs employ C2H2 zinc finger domains to bind DNA, motifs that are among the most capable of binding nucleosomal DNA (Zhu et al., 2018). GLI^A TFs have been shown to activate gene expression through interactions with chromatin remodelers, including the SWI/SNF complex in the developing limb bud and in Hh-dependent cancers (Jagani et al., 2010; Jeon and Seong, 2016; Shi et al., 2016; Zhan et al., 2011), as well as histone modifying complexes (Lex et al., 2020; Malatesta et al., 2013; Mazzà et al., 2013; Nye et al., 2014; Shi et al., 2014). Our observations also implicate GLI TFs in signal-dependent recruitment of chromatin remodeling complexes to the GLI1 GRN during heterochronic control of cardiac differentiation.

The concept of heterochrony was originally applied in evolutionary biology to explain the ontogeny of distinct morphological features between species (Smith, 2003). Heterochrony may play such a role in the evolution of heart development. Cardiac structures generated by the FHF, such as the left ventricle, are evolutionarily ancient compared to those generated by the SHF, such as the right ventricle, pulmonary outflow tract, and the atrial septum (Kelly, 2012). SHF-derived structures are predominately required for the efficient handling of pulmonary circulation, and interestingly, the lungs are the source of Hh ligand received by the SHF CPs (Goddeeris et al., 2008; Hoffmann et al., 2009). Activation of the GLI1-dependent GRN *in vivo*, in coordination with other critical progenitor-specific signaling pathways such as retinoic acid signaling (Li et al., 2010; Rankin et al., 2021), appears to prevent the premature emergence of the CM gene expression program and thereby delay cardiomyocyte differentiation. We speculate that Hh/GLI signaling may have been deployed during cardiopulmonary evolution as a heterochronic mechanism in lunged animals, delaying SHF differentiation to enable morphogenesis of the cardiovascular structures required for efficient cardio-pulmonary circulation. In this way, differentiation timing controlled by cell non-autonomous Hh signaling provides a plausible mechanism for inter-organ coordination of heart and lung development during evolution. We further speculate that Hh-dependent heterochronic GRNs may have been similarly deployed across contexts to delay lineage-specified progenitor differentiation and coordinate the evolution of complex organ development.

Limitations of the study

We have chosen to engineer mESC lines to overexpress either GLI1, an obligate activator modeling GLI^A TFs, or $GLI3^R$, the truncated repressor form of GLI3 modeling GLI^R TFs, to avoid the complications of post-translational GLI protein truncations (Dai et al., 1999; Hui and Angers, 2011; Lee et al., 1997; Ruiz i Altaba et al., 2007). This simplification does not consider specific contributions of GLI2 or complex GLI interactions. Attempts to study the activity of an embryonic signaling pathway *in vitro* are unavoidably limited by overly-simplistic models of intercellular communication. Overexpressing GLI1 or $GLI3^R$ *in vitro* does not fully model the complex signaling pathway interactions of the pSHF (Rochais et al., 2009). Furthermore, we focused on the pSHF, which avoids interactions with the neural crest that may affect anterior SHF differentiation dynamics.

Star Methods

RESOURCE AVAILABILITY

Lead contact—Further information and requests for resources and reagents should be directed to and will be fulfilled by the lead contact, Ivan Moskowitz (imoskowitz@peds.bsd.uchicago.edu).

Materials availability—Unique materials generated in this study, including plasmids and transgenic mouse embryonic stem cell (mESC) lines are available from the lead contact without restriction.

Data and code availability

- Drop-seq, RNA-seq, ChAP/ChIP-seq and ATAC-seq data have been deposited at GEO and are publicly available as of the date of publication. The accession number is listed in the key resources table.
- This paper does not report original code.
- Any additional information required to reanalyze the data reported in this paper is available from the lead contact upon request.

EXPERIMENTAL MODEL AND SUBJECT DETAILS

Mice—Mouse experiments were completed according to a protocol reviewed and approved by the Institutional Animal Care and Use Committee of the University of Chicago, in compliance with the USA Public Health Service Policy on Humane Care and Use of Laboratory Animals. Barrier mice were housed in a pathogen-free facility with positively pressurized individually ventilated cage racks and work is completed in biological safety cabinets. Caging and bedding were autoclaved prior to use and changed once per week, and new cages were provided with irradiated food and acidified water. A maximum of 5 adult mice were housed per cage. Animals were monitored daily for normal husbandry and any health concerns. Cages were kept under a 12-hour light and 12-hour dark cycle. CD1 mice were obtained from Charles River Laboratories. The $Shh^{-/-}$ mouse line was obtained from the Jackson laboratory. The $Osr1^{eGFPCre\text{-}ERT2}$ (Mugford et al., 2008) and $ROSA26^{Gli3R\text{-}Flag}$ (Vokes et al., 2008) lines were reported previously. All mouse alleles were maintained on

a mixed genetic background. All experiments were performed with at least N=2 mice or embryos per condition of mixed sexes. For crosses involving the *Osr1*$^{eGFPCre\text{-}ERT2}$ allele, mice were treated with 2mg tamoxifen, administered via IP injection at E7.5, E8.5 and E9.5. Embryos were harvested at E10.0, E10.5 or E14.5.

Transgenic mouse embryonic stem cell (mESC) lines—To generate inducible GLI1 or GLI3^{R} mouse embryonic stem cell (mESC) lines, the coding sequence for mouse *Gli1* or the truncated repressive form of *Gli3* (*Gli3*^{R}) was inserted in-frame with a Flag-Tev-Avi (FTA) tag into the *Hprt* locus of A2Lox.cre mES cells using a method previously described (Iacovino et al., 2011). Individual clones were assessed for differentiation potential and doxycycline-inducibility. One clone was selected and used for all experiments described herein, and all experiments were performed at the same passage number. mESC lines were passaged every 2 days on gelatin-coated dishes in stem cell maintenance media containing 1uM PD0325901 (Selleck Chemicals #S1036), 3uM CHIR-99021 (Selleck Chemicals #CT99021) and 1000 units LIF (Millipore Sigma #ESG1106), as previously described (Kattman et al., 2011).

METHOD DETAILS

CD1 embryo Drop-seq analysis—SHF and HT tissue was microdissected from E10.5 CD1 embryos. Tissue from 40 embryos was pooled to generate Replicate 1 and tissue from 45 embryos was pooled to generate Replicate 2. Tissue was dissociated for 5 minutes at 37°C in TrypLE Express Enzyme reagent (Thermo Fisher 12604013), with shaking. The dissociation reagent was quenched with 10% FBS, and cells were subsequently washed in a 0.01% BSA/PBS solution. Two single cell RNA-seq libraries were generated using the standard Drop-seq protocol (Macosko et al., 2015) with minor modifications. Briefly, cells were filtered using a 40 μm mesh filter (Nalgene, USA) and suspended in 1x PBS and 0.01% BSA at a concentration 120,000/mL. Custom-synthesized Drop-seq barcode (BC) beads (Chemgenes, USA) at 100,000/mL were likewise filtered trough 100 μm mesh filter and suspended in Drop-seq Lysis Buffer. Using 3 mL syringes for each, the solutions were co-encapsulated in monodisperse droplets of 125 μm in an inert carrier oil (BioRad Evagreen) using microfluidic device fabricated in-house. The cells underwent lysis in the microfluidic droplets and the mRNA were captured onto the BC beads via polydT oligoes affixed to the BC beads. The droplets were then broken to retrieve the BC beads with mRNA hybridized onto them in high salt solution that stabilized the BC oligo+mRNA complexes. The beads are thoroughly washed and reverse transcription is performed to convert the BC+mRNA complex into barcoded cDNA. An Exonuclease I digestion is performed to digest any barcodes that are unbound to mRNA. PCR of 12–15 cycles is performed to amplify the barcoded single cell library, quantified and the quality of cDNA library is assessed. Sequencing libraries are prepared using Illumina Nextera kit with sample-specific indices added that allow de-multiplexing each sample from sequence data. The samples were sequenced on the Illumina NextSeq platform using a 75 cycle kit, with a custom Read1 primer (Macosko et al., 2015). The two biological replicates were processed on different days.

Data processing.: Raw sequencing data were processed through a bioinformatics pipeline using STARsolo as aligner (Dobin et al., 2013) which we previously described (Selewa et al., 2020). Briefly, sequencing reads were aligned to the mouse reference genome (mm10) (Kent et al., 2002), and transcripts counts were quantified for each cell and gene. The pipeline is available here: https://github.com/aselewa/dropseqRunner. Data QC and the majority of the Drop-seq analysis was performed using the Scanpy (Wolf et al., 2018) software package (scanpy V1.5.1 and anndata V0.7.3). Cells from both biological replicates were combined after removing cells with fewer than 1,100 detected genes and genes that were detected in fewer than 5 cells in each. We also excluded cells with more than 7,000 genes to avoid counting cell doublets and cells with more than 3% of reads mapped to mitochondrial genes indicative of low quality. This resulted in a final set of 3,824 high quality cellular transcriptomes. Read counts in each cell were normalized to a total of 10,000 reads and log transformed.

Clustering and cell type identification.: We used an iterative analysis strategy to first identify all cell types within our dataset of cells from the SHF and then repeating this filtering cardiac-associated cell types. We then repeated this process on a selected subset of cells corresponding to those with an atrial CM fate. First, we identified highly variable genes within the cell populations using *highly_variable_genes()* with default parameters (min_mean = 0.0125, max_mean = 3, min_disp = 0.5), followed by scaling and PCA to calculate the first 75 principal components. Prior to clustering and non-linear dimensionality reduction, a neighborhood graph was constructed using *neighbors()* with *n_neighbors=15* and *n_pcs=35.* We calculated both UMAP and tSNE representations for all subsets of the data and chose the representation that best facilitated the visualization of the independently derived clusters. Graph-based clustering was performed using the Leiden algorithm (Traag et al., 2019) with *resolution = 1.* We identified marker genes for each of the 19 original clusters applying *rank_genes_groups()* with *method = 'logreg'* and used them to assign cell types (Table S1; Figure S1D–E). All cardiac related cell types were then selected for further analysis to ensure that no CM cells were lost (clusters: pSHF1, pSHF2, aSHF/pharyngeal arch mesoderm, cardiomyocytes, septum transversum, pro-epicardium/SA node), yielding a subset of 1,402 cells (Figure S1D–F and Table S1). The entire analysis process was then repeated for this subset with the following modifications: Only the first 12PCs were used for clustering and dimensionality reduction and resolution was set to 0.3 for clustering with the Leiden algorithm. This procedure yielded 7 clusters representing cells in several cardiac lineages, which we further filtered to retain only cells definitively corresponding to the atrial CM lineage (*Gata4*$^+$, *Nkx2–5*$^+$, *Tbx5*$^+$, *Tnnt2*$^+$) (de Soysa et al., 2019; Han et al., 2019). This step excluded cells corresponding to the aSHF (*Tbx1*$^+$, *Fgf10*$^+$), the septum transversum (*Wt1*$^+$) and the pro-epicardium/SA node (*Tbx18*$^+$) (Figure S1G–H). Neighborhood graph, clustering and dimensionality reductions (UMAP,TSNE) were re-calculated for this subset using the first 8 PCs and cluster resolution 0.2. This final atrial CM-associated subset contained 846 cells sorted into 4 distinct clusters (Figure 1C–D and Table S1). We confirmed the left/right side-specificities of the two progenitor clusters (CP1 and CP2) by examining the expression of *D030025E07Rik* (right side marker) and *Pitx2* (left side marker) in the wild type pSHF *in vivo* (Figure S2C–D). Significance was assessed using a two-sided T-test on the raw counts.

Pseudotime.: To calculate the differentiation pseudotime we first computed a diffusion map using *diffmap()* with *n_comps=15* and default settings (Haghverdi et al., 2016). To identify a starting cell for the pseudotime calculation, we calculated a 'differentiation score' by computing the mean expression of know cardiac marker genes for each cell (Table S1) (de Soysa et al., 2019) and chose as the root cell the most differentiated cell according to this metric. Diffusion pseudotime was calculated using *dpt*() with *n_dcs*= 6 and default settings. We thus use 1-pseudotime to describe the pseudotime associated with the developmental progression. We chose this approach to overcome the larger heterogeneity within the progenitor population, which made choosing a progenitor root cell more difficult.

Differential Expression, cell cycle and signaling pathway scores.: Cell cycle scores were calculated as previously described (Tirosh et al., 2016) after converting the human gene symbols to the corresponding symbols for the orthologous mouse genes. To confirm the identities of CPs and CMs, we identified differentially expressed genes using the *FindMarkers* function in the Seurat v4 R package (Hao et al., 2021) with default settings and a Wilcoxon Rank Sum Test (Table S1), we retained genes with adjusted p-value <= 0.05 and |log2 fold change| >= 0.5. Analysis for enriched GO terms was performed using Metascape (Zhou et al., 2019). To map activity of developmental signaling pathways, we obtained sets of target genes from 6 developmental pathways (Han et al., 2019) and used the aggregate expression in each cell as a proxy for pathway activity. The following target genes were included for each pathway: Hedgehog signaling ('Gli1', 'Ptch1', 'Foxf1', 'Foxf2', 'Hhip'), Retinoic acid signaling ('Hoxa1', 'Hoxa2', 'Hoxa3', 'Hoxb1', 'Hoxb2', 'Hoxb3', 'Cyp26a1', 'Hnf1b', 'Rarb'), Wnt signaling ('Axin1', 'Lef1', 'Axin2', 'Myc', 'Sp5', 'Ccnd1', 'Dkk1', 'Notum'), Fgf signaling ('Spry1', 'Spry2', 'Spry4', 'Dusp6', 'Etv4', 'Etv5', 'Fos', 'Myc',' Junb', 'Dusp14'), Notch signaling ('Hes1', 'Hey1', 'Hey2', 'Dll4', 'Heyl', 'Notch1', 'Notch3', 'Hes5', 'Nrarp') and Bmp signaling ('Msx1', 'Bambi', 'Smad7', 'Id1', 'Id2', 'Id3', 'Id4', 'Bmper', 'Msx2').

Data visualization in heatmaps.: To display the general trends expression patterns of these genes at the single cell level, we denoised the single cell expression measurements using the computational algorithm ENHANCE that relies on principal component analysis in order to separate biological variation from technical noise (Wagner et al., 2019). Denoised single cell gene expression values were displayed with heatmaps using the R package ComplexHeatmaps (Gu et al., 2016). These heatmaps were used to capture and display expression patterns during differentiation from CP to CM. Columns represent cells sorted based on their pseudotime rank. Rows correspond to different selected gene sets and differend by heatmap. Hierarchical clustering was used to sort genes by similarity of their temporal expression patterns. Gene expression and pathway scores were also displayed as line graphs using the ggplot package in R.

***Shh*$^{-/-}$ embryo transcriptome profiling—**The pSHF was microdissected from five individual E10.5 *Shh*$^{+/+}$ and five *Shh*$^{-/-}$ embryos for bulk RNA-seq analysis, and yolk sacs were collected for genotyping. Tissues were mechanically homogenized in TRIzol Reagent (ThermoFisher Scientific 15596026), and RNA was isolated using RNeasy Mini RNA Isolation Kit (Qiagen 74104). 1ug of total RNA was then used to generate sequencing

libraries using the TruSeq RNA Sample prep kit v2 (Illumina RS-122–2001), as per recommended instructions. Libraries were quantitated on an Agilent Bio-Analyzer and pooled in equimolar amounts. Pooled libraries were sequenced on the HiSeq2500 in Rapid Run Mode following the manufacturer's protocols to generate stranded single-end reads of 50bp. The number of sequenced reads per sample ranged between 11.7 million 17.7 million with an average of 15 million sequenced per sample. Quality control for raw reads involved trimming the first 13bp with FastQ Groomer to ensure a median quality score of 36 or above for each sample. Fastq files were aligned to the UCSC mouse genome (mm9) (Kent et al., 2002) using TopHat (Cole Trapnell, 2009) (version 2.0.10) with the following parameters: (--segment-length 19 --segment-mismatches 2 --no-coverage-search). Between 11.4 million 17.2 million successfully mapped reads were then merged. One $Shh^{+/+}$ sample was discarded due to discordance with all other samples. Beyond PCA analysis, we did not examine individual samples for consistency of gene expression, which should reflect consistency in microdissection technique, representing a potential limitation of this study. Remaining samples were then analyzed for differential gene expression using Cuffdiff (Trapnell et al., 2013) (version 2.1.1) with quartile normalization. Significantly differentially expressed genes were identified using thresholds of FDR <0.05 and fold change > 1.5, resulting in 204 activated and 52 repressed genes, in the $Shh^{-/-}$ pSHF samples relative to $Shh^{+/+}$ samples. Differential expression of selected genes identified by RNA-seq was validated using qPCR. RNA was harvested from $Shh^{+/+}$ and $Shh^{-/-}$ pSHF samples with a Nucleospin RNA extraction kit (Machery-Nagel 740955.250). RNA was then used to perform one-step qPCR with the iTaq One-Step system (Bio-Rad 1725151), and expression levels in mutant samples were normalized to $Shh^{+/+}$ samples. GO term analysis was performed as described above. To intersect *Shh*-dependent genes with differentiation stage-dependent gene expression, we also performed bulk RNA-seq analysis on wild type embryonic tissues. The pSHF and HT from six CD1 embryos was microdissected and RNA-seq analysis was performed as above to identify genes differentially expressed between the two tissues (fold change > 1.5, FDR < 0.05). Additional data analysis and visualization was performed in R.

mESC cardiomyocyte differentiation culture and GLI1 OE experiments—mESCs were maintained and differentiated into CMs as previously described (Kattman et al., 2011). RNA was collected and qPCR was performed as above to assess the expression of CP markers *Tbx5, Nkx2–5* and *Isl1*, as well as Hh markers *Gli1*, and *Ptch1* relative to *Gapdh* in differentiating CMs. For western blots, protein was harvested with cell lysis buffer (Cell Signaling 9803), and 20–40 ug was loaded onto 4–15% pre-cast gels (Bio-Rad 17000546) and run using the Bio-Rad Mini-PROTEAN Tetra Cell system. Blots were probed with antibodies recognizing GLI1 (1:1,000; Cell Signaling 2534S), GLI3 (1:1,000; R&D AF3690) and GAPDH (1:10,000; Abcam ab8245). Pixel density for GLI1/3 was then computed, relative to the pixel density of GAPDH, using ImageJ (Schneider et al., 2012). The relative densities of GLI1/3 at various mESC-CM differentiation stages were summed, and the proportion of density contributed at each stage by GLI1 (GLI^A) and GLI3 (GLI^R) was calculated.

RNA was harvested from *in vitro* samples at D5, D6, D7, D8, D10 and D15 of the mESC-CM differentiation with a Nucleospin RNA extraction kit (Machery-Nagel 740955.250). RNA-seq was performed on three replicate samples for each time point using the TruSeq RNA Sample library prep kit v2 (Illumina RS-122-2001), sequencing on a HiSeq4000 instrument in Rapid Run Mode to generate single-end reads of 50bp. Reads were aligned to mouse genome and transcriptome mm10 from UCSC with parameter --quantMode GeneCounts to retrieve exon counts. E10.0 pSHF and HT RNA-seq data, plus publicly available adult mouse heart RNA-seq data (Akerberg et al., 2019) were then compared to the *in vitro* time series. Raw counts from both *in vitro* and *in vivo* samples were batch corrected with Combat-seq function from R CRAN package SVA. Normalization was performed with DESEq2 ‘s vst function. Normalized counts were then summarized into principal components with Bioconductor package PCAtools. We used the top 500 most variable genes for visualization and added the top ten loadings from PC1 as labels. The same 500 genes were then clustered and scaled with R package pheatmap. For confidence estimates of hierarchical clustering results, counts were first normalized by DESEQ2 function vst() and extracted with assay(). We used R CRAN package pvclust (Suzuki and Shimodaira, 2006) to calculate the p-values from each cluster resulting from hierarchical clustering. P-values are based on multiscale bootstrap resampling from 10,000 bootstraps. Dendogram was visualized with R package Dendextend. Significant *P*-values are those were au values (in red to left of branch point) are > 95.

Attempts to study the activity of an embryonic signaling pathway *in vitro* are unavoidably limited by imprecise comparisons and overly-simplistic models of protein behavior. For example, overexpressing GLI1 or $GLI3^R$ in mESC-CPs *in vitro* does not fully model the complex signaling milieu of the pSHF and any potential pathway interactions therein (Rochais et al., 2009). Overly high levels of GLI1 expression *in vitro* can also lead to spurious dysregulation of gene expression and aberrant cell behaviors that do not reflect GLI1 function in the pSHF. Additionally, a focus on GLI1 or $GLI3^R$ function means that we ignore the contributions of GLI2 to the regulation of Hh target genes. We have thus carefully considered these caveats and devised a system that we believe accurately describes the molecular function of GLI1 in CPs. 1) We have chosen to engineer mESC lines to overexpress either GLI1, an obligate activator modeling GLI^A TFs, or $GLI3^R$, the truncated repressor form of GLI3 modeling GLI^R TFs, to avoid the complications of post-translational GLI protein truncations (Dai et al., 1999; Hui and Angers, 2011; Lee et al., 1997; Ruiz i Altaba et al., 2007). 2) We have chosen to overexpress GLI1 and $GLI3^R$ at a transcriptional stage in the *in vitro* mESC-CM differentiation time series that most closely mirrors the transcriptional state of the pSHF with the goal of ensuring that GLI1 cofactors and other interactors are present (see section above). 3) We have tested multiple dosages of doxycycline to find the dose that most accurately represents Hedgehog activity in the pSHF. Expression of the Hh target, *Foxf1*, was quantified relative to *Gapdh* expression in cells treated with increasing concentrations of doxycycline and relative to *Gapdh* in pSHF embryo samples. Based on results from these assays, a final doxycycline concentration of 500ng/ml was chosen for all GLI1 OE experiments because this dose caused relative *Foxf1* expression in mESC-CPs to match its relative expression in the pSHF. 4) Finally, our *in vitro* studies are corroborated by data collected from *in vivo* CP and CM samples, suggesting that

our mESC-CP GLI1 OE system models Hh activity in SHF cardiomyocyte differentiation reasonably well.

For all GLI1 overexpression (GLI1 OE) experiments, doxycycline (Sigma D9891) was added to cultures at the CP stage (D5). Cells were then washed and media was changed after 24hrs of exposure to doxycycline. qPCR and western blots were performed, as described above, on D6 samples to assess the expression level of *Gli1* and Hh targets, relative to untreated controls. Western blots for GLI1-FTA were probed with antibodies recognizing the FLAG epitope (1:1,000, Sigma F3165, M2) and GAPDH (as above). mESC immunofluorescence was performed on control and GLI1 OE CMs with an antibody recognizing cardiac Troponin T (cTnT, 1:100, ThermoFisher Scientific MS-295-P1). The area of cTnT positivity was calculated as the mean grey area / mm^2 of 5 fields of view across two biological replicates per condition, using the threshold measurement tool in ImageJ. The percentage of cTnT+ cells was calculated by dissociating D8 or D10 CMs and staining with a BV421-conjugated anti-cTnT antibody (BD Biosciences 565618, Lot 8136651, 13–11, 1:100) for 1 hour at 4°C. The fluorescent signal from GLI1 OE and control cell samples stained for cTnT-positivity was normalized to fluorescent signal from cells stained with a BV421-conjugated isotype control IgG antibody (BD Biosciences 562438, Lot 8242926, X40, 1:100). Fluorescence was quantified, and cells were counted on a BD LSRFortessa 4–15 HTS FACS instrument at the University of Chicago's Cytometry and Antibody Technology core facility. The number of beating foci was calculated as the average number of independently beating regions within 5 fields of view across two biological samples, counted from 5 second videos taken on a Zeiss Axiovert 200m inverted widefield microscope at the University of Chicago's Integrated Light Microscopy core facility. Indirect FACS analysis for Ki-67+ cells was performed using a primary antibody recognizing Ki-67 (ThermoFisher 14-5698-80, SolA15, 1:100), and a secondary antibody conjugated to Alexa Fluor 594 (ThermoFisher A-11007, 1:1000). Fluorescence was quantified, and cells were counted on an Agilent NovoCyte Penteonn FACS instrument at the University of Chicago's Cytometry and Antibody Technology core facility.

RNA-seq was performed at D6, D8 and D12 of mESC-CM differentiations with at least two replicate GLI1 OE and control samples per stage, as described above. Reads were mapped to the mouse genome (mm9) (Kent et al., 2002) with Bowtie2 (Langmead and Salzberg, 2012) and transcripts were assigned and quantified with Cufflinks with default parameters (Trapnell et al., 2010). Reads were then normalized and differentially expressed genes for each timepoint were identified with edgeR (Mark D. Robinson, 2010). Differentially expressed genes were then filtered to include only genes with a $\log_2$ fold change ≥ 0.5 and an FDR ≤ 0.05. GO term analysis on D6 dysregulated genes, and qPCR validation of selected genes, was performed as described above.

Identification of GLI1 and $GLI3^R$ direct targets in CPs—The GLI1-FTA cell line was used to identify GLI1 binding sites, and the $GLI3^R$-FTA cell line was used to identify $GLI3^R$ binding sites in CPs. Cells at the CP stage (D5) were treated with doxycycline (500 ng/ml) for 24 hours and harvested at D6. ChAP-seq was performed as previously described for ChIP-seq (Ikegami et al., 2020), with minor modifications. Briefly, 2×10^6 cells were cross-linked in 1% PFA for 5 minutes at room temperature, with rocking. The reaction

was then quenched with 125 mM glycine. The cross-linked tissues were incubated in LB1 (50 mM HEPESK-OH, pH 7.5, 140 mM NaCl, 1 mM EDTA, 10% Glycerol, 0.5% NP-40, 0.25% Triton X-100) with protease and phosphatase inhibitors on ice for 10 minutes. The tissues were then sonicated in LB3 (10 mMTris-HCl, pH 8.0, 100 mM NaCl, 1 mM EDTA, 0.5 mM EGTA, 0.1% sodium deoxycholate, 0.5% N-lauroyl sarcosine, 1% Triton X-100) with protease and phosphatase inhibitors for 5 minutes at 4°C. Chromatin extract was then cleared by centrifugation at 14,000g, 4°C for 10 minutes. To pull-down GLI1-FTA or $GLI3^{R}$-FTA, the chromatin extract was incubated with 50ul M-280 Streptavidin-conjugated magnetic beads (Life Technologies, 11205D) for 30 minutes at room temperature with rotation, washed in sequence by LB3, LB3 with 1 M NaCl, LB3 with 0.5 M NaCl, LB3, and TE (10 mM Tris-HCl, pH 8.0, 1 mM EDTA). For ChIP-seq of H3K27ac-enriched chromatin, extract was incubated with 1ul anti-H3K27ac antibody (FUJIFILM Wako 306–34849) at 4°C overnight, then incubated with 50ul Protein G Dynabeads for 4 hours at 4°C, followed by washes (see above). The captured chromatin, and input samples, were eluted in ChIP Elution Buffer (10 mM Tris-HCl, pH 8.0, 1 mM EDTA, 1% SDS, 250 mM NaCl) at 65°C. For both ChAP-seq and ChIP-seq, DNA was purified after RNase and proteinase K treatment and reversing cross-links.

High-throughput sequencing libraries from ChAP/ChIP and input DNA were prepared using the NEBNext Ultra DNA Library Prep Kit (New England Biolabs, E7370S). During library preparation, adaptor-ligated DNA fragments of 200–650 bp in size were selected before PCR amplification using Ampure XP magnetic beads (Beckman Coulter, A63880). DNA libraries were sequenced using Illumina Hi-seq instruments (single-end 50 base) by the Genomics Core Facility at the University of Chicago. Reads were aligned to mouse genome mm10 (Kent et al., 2002) from UCSC with Bowtie2 v2.3.2. Reads with a phred score less than 30, aligned to mitochondrial genome and clone contigs were removed with Samtools v1.5. Reads were sorted with Samtools sort by genomic location before removing duplicates with picardtools MarkDuplicates v2.8.1 with default settings (http://broadinstitute.github.io/picard). Peaks were called on uniquely mapped reads with macs2 (v2.1.1 settings -f BAM -g mm -B -q 0.05), grouping together both replicates as well as calling peaks on individual samples. Consensus peaks were determined by intersecting individual peak calls with Homer mergePeaks v4.1.1. Consensus peak summits were determined by intersecting the consensus peak regions with the summit file from the grouped peak calls. Coverage file (bigwig) was generated with Macs2 (Zhang et al., 2008) using the bdgcmp function (-m FE) followed by bedGraphToBigWig v4 from UCSC.

Chromatin accessibility profiling of GLI1-FTA mESC-CPs and embryonic tissues—Assay for transposase-accessible chromatin was performed as previously described (Buenrostro et al., 2013). Briefly, the pSHF and HT were microdissected from CD1 embryos, pooled, and dissociated with TrypLE (ThermoFisher Scientific 12605–010). For D5 and D7 GLI1 OE and control mESC samples, 150,000 cells per sample were collected for each condition. Embryo and cell samples were then lysed, as described (Buenrostro et al., 2013), and transposition was carried out at 37C for 30 minutes with Illumina's Nextera DNA Library Prep kit (Illumina, FC-131-1096). Libraries were generated from transposed DNA and sequenced on an Illumina HiSeq4000 instrument in

the University of Chicago's Genomic Facility. Data were analyzed with FastQC (Andrews, S., 2010) and mapped to the mouse genome (mm9) with Bowtie2 using default parameters (Langmead and Salzberg, 2012). Peaks were called for all samples with MACS2 (Zhang et al., 2008) using the following parameters: -q 0.05 --nomodel --shift -100 --extsize 200 --nolambda --keep-dup all –call-summits. Peak sets from biological replicates were overlapped with Bedtools intersect (Quinlan and Hall, 2010) to identify replicated peaks. Peaks sets generated from regions present in both replicates were then intersected to identify peaks specific to each tissue type. Normalized reads were visualized on the UCSC genome browser (Kent et al., 2002). For D5 and D7 *in vitro* samples, we made a consensus set of open chromatin regions with the ATAC-seq summit peak calls. Homer function mergePeaks (-d 200) was used to combine the summits within 200 bp of each other. Promoters from defined GLI1 GRN genes were extended by 200 kb and overlapped with consensus regions to mark putative enhancer elements of these genes. R package ComplexUpset was used to generate upset plot in Figure 5F.

Immunoblotting—Wild type E10 embryos were harvested from two pregnant CD1 females. Embryos tissues corresponding to the pSHF, aSHF and HT were microdissected as previously (Hoffmann et al., 2014), pooled and lysed. 35ug of total protein was used for western blot analysis of each tissue. Blots were probed with antibodies recognizing GLI1 (1:1,000; Cell Signaling 2534S), GLI2 (1:1,000; Cell Signaling 2585S), GLI3 (1:1,000; R&D AF3690) and GAPDH (1:10,000; Abcam ab8245). For each transcription factor, pixel density was then computed in all tissues, relative to the pixel density of GAPDH within that tissue, using ImageJ (Schneider et al., 2012). Finally, the relative densities of transcription factors for the pSHF and HT were summed, and the proportion of density contributed to each tissue by GLI^A (GLI1, $GLI2^A$, $GLI3^A$) and GLI^R ($GLI2^R$ and $GLI3^R$) was calculated.

Luciferase Assays—Expression vectors for *Gli1*, *Gli3T* and *Tbx5* and a luciferase vector containing the *Fox* enhancer were previously described (Hoffmann et al., 2014). Expression and reporter vectors were transfected into HEK293T cells using FuGENE HD (Promega E2311). Cells were cultured for 48 hours after transfection, then lysed and assayed using a Dual-Luciferase Reporter Assay system (Promega E1960).

Transient transgenics—The *Foxf1a* enhancer and minimal promoter used in the luciferase assays were subcloned from the pENTR vector into the Hsp68-LacZ vector (Kothary et al., 1989) using the Gateway system (Invitrogen). GLI binding sites were mutated using the Agilent QuikChange Multi site-directed mutagenesis kit (Agilent 210515–5). The resulting constructs were digested with NotI enzyme to remove the pBlueScript backbone, gel-purified, injected into fertilized mouse eggs at the University of Chicago Transgenics Core Facility and implanted into female mice. Embryos were harvested at E9.5 and stained as described previously (Hoffmann et al., 2014).

Embryo Immunofluorescence & Histology—Embryos were harvested from timed pregnancies and yolk sacs were collected for genotyping. For $Osr1^{eGFPCre\text{-}ERT2/+}$; $ROSA26^{Gli3R\text{-}Flag/+}$ ($Gli3^R$ OE) embryos, pregnant female mice were administered 2 mg tamoxifen at E7.5, E8.5 and E9.5 ($Gli3^R$ OE) by intraperitoneal injection. Embryos were

then harvested at E10.5 for immunofluorescence studies, or at E14.5 for histological examination. For immunofluorescence, E10.5 embryos were fixed overnight in 4% paraformaldehyde, washed with PBS and processed for paraffin sectioning. 5um serial sections were generated and used for immunofluorescence with primary antibodies recognizing sarcomeric myosin (1:20, DSHB MF20) or MYL7 (1: 500, ThermoFisher 17283-1-AP) and Alexa Fluor-conjugated secondary antibodies (1:1000, Thermo Fisher Scientific). Antigen retrieval was performed on all sections with 10mM sodium citrate buffer. DAPI was used to counterstain tissues and provide a tissue reference. Sections were imaged with an Olympus IX81 inverted widefield microscope using 10x and 20x objectives in the University of Chicago's Integrated Light Microscopy Core Facility. Images were processed with ImageJ.

Histological studies were performed at E14.5. Embryos were harvested and fixed in 4% paraformaldehyde overnight at 4°C, and then processed for paraffin sectioning. 5um sections were then stained with hematoxylin and eosin to reveal the structural morphology of the atrial septum in mutant and control embryos.

Bioinformatic analysis of developmental time series RNA-seq data—Publicly available data sets from human and mouse were downloaded (Table S6), and grouped by tissue, germ layer of origin and developmental stage. We used TPMs generated by the Encode Consortium, and these expression values were further ranked per gene so as to eliminate possible batch effects with function percent_rank from R Bioconductor package dplyr. Ranked expression values of *Gapdh* and *Gli*1 were then visualized into boxplots with function geom_boxplot from R Bioconductor package ggplot2. We used R base function aov to perform an ANOVA test to find significant differences in expression between all developmental stage points, followed by R base function TukeyHSD to find statistically significant differences between two time points. We performed differential expression tests between all mouse progenitor and mouse differentiated tissues described above using expected counts generated by Encode with Bioconductor package DESeq2. We determined progenitor-enriched genes as those with adjusted *P*-values less than 0.05 and $\log^2$ fold change less than −1. We then used R biocondcutor package clusterProfiler to find KEGG pathways enriched in progenitor-enriched genes, and visualized with ggplot2 as above.

mESC neuronal differentiation culture and GLI1 OE—Neuron differentiation was performed as previously described (Cai and Grabel, 2007; Ying et al., 2003). Briefly, cells were plated at a density of 9.5×10^4 /cm^2 on a 0.1% gelatin-coated dish and allowed to differentiate in N2B27 medium, which was replaced every two days. RNA was collected and qPCR was performed as described above to assess the expression of neural stem cell marker *Sox1*, neural progenitor markers *Nestin* and *Pax6* and neuron marker *Tubb3,* as well as Hh markers *Gli1*, *Hhip* and *Ptch1* relative to *Gapdh* in differentiating neurons.

For GLI1 overexpression experiments, 500ng/ml doxycycline (Sigma D9891) was added to cultures at the neural progenitor stage (Day 3). Cells were then washed and media was changed after 48hrs of exposure to doxycycline. The number of axons and the number of neurospheres / neural rosette clusters were manually counted by two independent observers blinded to the treatment from ten fields of view across two biological replicates using

10x brightfield microscopy (Olympus IX81). mESC immunofluorescence was performed on control and GLI1 OE cells with an antibody recognizing β-Tubulin III (*Tubb3*/TUJ1, 1:100, R & D Systems MAB1195). The area of TUJ1 positivity was calculated as the mean grey area / mm^2 of 5 fields of view across two biological replicates per condition, using the threshold measurement tool in ImageJ. RNA-seq, and qPCR validation, was performed with mESC neural GLI1 OE and control samples at D5 and D10 in a similar manner as for mESC cardiac samples, as above.

QUANTIFICATION AND STATISTICAL ANALYSIS

All statistical tests were performed in R. Data are summarized and presented as mean +/− SEM. Shapiro-Wilk's and Levene's tests were used to determine whether data met the assumptions of parametric statistical tests. If data met the assumptions, a two-sided Student's *t*-test between two groups or ANOVA between multiple groups was performed to determine whether differences between the groups were statistically significant. ANOVA was followed by post-hoc Tukey tests to identify pairwise differences. If assumptions were not met, a Welch's *t*-test, Kruskal-Wallis rank sum test or Wilcoxon signed-rank test were performed instead. Proportions were compared and enrichment calculated using the Fisher's Exact test. * $p < 0.05$; ** $p < 0.01$; *** $p < 0.005$; **** $p < 0.001$. Detailed information regarding statistical tests is included in the Results section. All data was plotted in R.

Supplementary Material

Refer to Web version on PubMed Central for supplementary material.

ACKNOWLEDGEMENTS

The authors are deeply grateful to the staff of the Genomics, DNA Sequencing, Integrated Light Microscopy, Cytometry and Antibody Technology and Human Tissue Resource Center core facilities at the University of Chicago. This work was supported by the NIH/NHLBI: R01 HL092153 (I.P.M), R01 HL124836 (I.P.M), R01 HL126509-02 (I.P.M), R01 HL147571-01 (I.P.M), NIH/NHLBI NRSA T32 HL007381-36/37 (M. R.) and NIH/NHLBI F32 HL136168-01 (M. R.). This work was also supported by the American Heart Association: AHA 13EIA14690081 (I.P.M.) and AHA Postdoctoral Fellowship 17POST33670937 (M. R.). I.P.M is grateful to Raghu and Rashida Mendu for their support of this project.

REFERENCES

Agathocleous M, Locker M, Harris WA, Perron M, 2007. A general role of hedgehog in the regulation of proliferation. Cell Cycle. 10.4161/cc.6.2.3745

Akerberg BN, Gu F, VanDusen NJ, Zhang X, Dong R, Li K, Zhang B, Zhou B, Sethi I, Ma Q, Wasson L, Wen T, Liu J, Dong K, Conlon FL, Zhou J, Yuan GC, Zhou P, Pu WT, 2019. A reference map of murine cardiac transcription factor chromatin occupancy identifies dynamic and conserved enhancers. Nat. Commun. 2019 101 10, 1–16. 10.1038/s41467-019-12812-3

Ambros V, Horvitz HR, 1984. Heterochronic mutants of the nematode Caenorhabditis elegans. Science 226, 409–416. 10.1126/science.6494891 [PubMed: 6494891]

Averbukh I, Lai SL, Doe CQ, Barkai N, 2018. A repressor-decay timer for robust temporal patterning in embryonic drosophila neuroblast lineages. eLife 7. 10.7554/eLife.38631

Bademci G, Abad C, Incesulu A, Elian F, Reyahi A, Diaz-Horta O, Cengiz FB, Sineni CJ, Seyhan S, Atli EI, Basmak H, Demir S, Nik AM, Footz T, Guo S, Duman D, Fitoz S, Gurkan H, Blanton SH, Walter MA, Carlsson P, Walz K, Tekin M, 2019. FOXF2 is required for cochlear development in humans and mice. Hum. Mol. Genet. 28, 1286–1297. 10.1093/HMG/DDY431 [PubMed: 30561639]

Balaskas N, Ribeiro A, Panovska J, Dessaud E, Sasai N, Page KM, Briscoe J, Ribes V, 2012. Gene Regulatory Logic for Reading the Sonic Hedgehog Signaling Gradient in the Vertebrate Neural Tube. Cell 148, 273–284. 10.1016/J.CELL.2011.10.047 [PubMed: 22265416]

Bax NAM, Lie-Venema H, Vicente-Steijn R, Bleyl SB, Van Den Akker NMS, Maas S, Poelmann RE, Gittenberger-de Groot AC, 2009. Platelet-derived growth factor is involved in the differentiation of second heart field-derived cardiac structures in chicken embryos. Dev. Dyn. 238, 2658–2669. 10.1002/dvdy.22073 [PubMed: 19705434]

Baydyuk M, Russell T, Liao GY, Zang K, An JJ, Reichardt LF, Xu B, 2011. TrkB receptor controls striatal formation by regulating the number of newborn striatal neurons. Proc. Natl. Acad. Sci. U. S. A. 108, 1669–1674. 10.1073/PNAS.1004744108/SUPPL_FILE/PNAS.201004744SI.PDF [PubMed: 21205893]

Beachy PA, Karhadkar SS, Berman DM, 2004a. Tissue repair and stem cell renewal in carcinogenesis. Nature. 10.1038/nature03100

Beachy PA, Karhadkar SS, Berman DM, 2004b. Tissue repair and stem cell renewal in carcinogenesis. Nature 432, 324–331. 10.1038/nature03100 [PubMed: 15549094]

Bedont JL, LeGates TA, Slat EA, Byerly MS, Wang H, Hu J, Rupp AC, Qian J, Wong GW, Herzog ED, Hattar S, Blackshaw S, 2014. Lhx1 Controls Terminal Differentiation and Circadian Function of the Suprachiasmatic Nucleus. Cell Rep. 7, 609–622. 10.1016/J.CELREP.2014.03.060 [PubMed: 24767996]

Belgacem Y, Hamilton A, Shim S, Spencer K, Borodinsky L, 2016. The Many Hats of Sonic Hedgehog Signaling in Nervous System Development and Disease. J. Dev. Biol. 4, 35. 10.3390/jdb4040035 [PubMed: 29615598]

Bergsland M, Werme M, Malewicz M, Perlmann T, Muhr J, 2006. The establishment of neuronal properties is controlled by Sox4 and Sox11. Genes Dev. 20, 3475–3486. 10.1101/GAD.403406 [PubMed: 17182872]

Bernstein BE, Stamatoyannopoulos JA, Costello JF, Ren B, Milosavljevic A, Meissner A, Kellis M, Marra MA, Beaudet AL, Ecker JR, Farnham PJ, Hirst M, Lander ES, Mikkelsen TS, Thomson JA, 2010. The NIH Roadmap Epigenomics Mapping Consortium. Nat. Biotechnol. 2010 2810 28, 1045–1048. 10.1038/nbt1010-1045

Bertrand N, Roux M, Ryckebüsch L, Niederreither K, Dollé P, Moon A, Capecchi M, Zaffran S, 2011. Hox genes define distinct progenitor sub-domains within the second heart field. Dev. Biol. 353, 266–274. 10.1016/j.ydbio.2011.02.029 [PubMed: 21385575]

Briggs LE, Burns TA, Lockhart MM, Phelps AL, van den Hoff MJB, Wessels A, 2016. Wnt/β-catenin and sonic hedgehog pathways interact in the regulation of the development of the dorsal mesenchymal protrusion. Dev. Dyn. 245, 103–113. [PubMed: 26297872]

Briggs LE, Kakarla J, Wessels A, 2012. The pathogenesis of atrial and atrioventricular septal defects with special emphasis on the role of the dorsal mesenchymal protrusion. Differ. Res. Biol. Divers. 84, 117–130.

Briscoe J, Pierani A, Jessell TM, Ericson J, 2000. A homeodomain protein code specifies progenitor cell identity and neuronal fate in the ventral neural tube. Cell 101, 435–45. 10.1016/s0092-8674(00)80853-3 [PubMed: 10830170]

Briscoe J, Thérond PP, 2013. The mechanisms of Hedgehog signalling and its roles in development and disease. Nat. Rev. Mol. Cell Biol. 14, 416–429. [PubMed: 23719536]

Brown SA, 2014. Circadian clock-mediated control of stem cell division and differentiation: beyond night and day. Development 141, 3105–3111. 10.1242/dev.104851 [PubMed: 25100653]

Bruneau BG, 2013. Signaling and transcriptional networks in heart development and regeneration. Cold Spring Harb. Perspect. Biol. 5, a008292. 10.1101/cshperspect.a008292 [PubMed: 23457256]

Buenrostro JD, Giresi PG, Zaba LC, Chang HY, Greenleaf WJ, 2013. Transposition of native chromatin for fast and sensitive epigenomic profiling of open chromatin, DNA-binding proteins and nucleosome position. Nat. Methods 10, 1213–1218. [PubMed: 24097267]

Cai C, Grabel L, 2007. Directing the differentiation of embryonic stem cells to neural stem cells. Dev. Dyn. 236, 3255–3266. 10.1002/DVDY.21306 [PubMed: 17823944]

Cai C-L, Liang X, Shi Y, Chu P-H, Pfaff SL, Chen J, Evans S, 2003. Isl1 identifies a cardiac progenitor population that proliferates prior to differentiation and contributes a majority of cells to the heart. Dev. Cell 5, 877–889. [PubMed: 14667410]

Carcagno AL, Di Bella DJ, Goulding M, Guillemot F, Lanuza GM, 2014. Neurogenin3 Restricts Serotonergic Neuron Differentiation to the Hindbrain. J. Neurosci. 34, 15223–15233. 10.1523/JNEUROSCI.3403-14.2014 [PubMed: 25392491]

Carden MJ, Trojanowski JQ, Schlaepfer WW, Lee VMY, 1987. Two-stage expression of neurofilament polypeptides during rat neurogenesis with early establishment of adult phosphorylation patterns. J. Neurosci. 7, 3489–3504. 10.1523/JNEUROSCI.07-11-03489.1987 [PubMed: 3119790]

Carroll JS, Liu XS, Brodsky AS, Li W, Meyer CA, Szary AJ, Eeckhoute J, Shao W, Hestermann EV, Geistlinger TR, Fox EA, Silver PA, Brown M, 2005. Chromosome-wide mapping of estrogen receptor binding reveals long-range regulation requiring the forkhead protein FoxA1. Cell 122, 33–43. 10.1016/J.CELL.2005.05.008/ATTACHMENT/E8EBBA-13-43AD-470C-B24D-04795CE939C6/MMC4.XLS [PubMed: 16009131]

Liu Chengyu, Liu Wei, Palie Jennifer, Mei Fang Lu Nigel A. Brown, Martin James F., 2002. Pitx2c patterns anterior myocardium and aortic arch vessels and is required for local cell movement into atrioventricular cushions | Development. Development 5081–5091. [PubMed: 12397115]

Cole Trapnell LPSLS, 2009. TopHat: discovering splice junctions with RNA-Seq | Bioinformatics | Oxford Academic. Bioinformatics 25, 1105–1111. [PubMed: 19289445]

Consortium TEP, 2012. An integrated encyclopedia of DNA elements in the human genome. Nature 489, 57–74. [PubMed: 22955616]

Creyghton MP, Cheng AW, Welstead GG, Kooistra T, Carey BW, Steine EJ, Hanna J, Lodato MA, Frampton GM, Sharp PA, Boyer LA, Young RA, Jaenisch R, 2010. Histone H3K27ac separates active from poised enhancers and predicts developmental state. Proc. Natl. Acad. Sci. U. S. A. 107, 21931–21936. 10.1073/pnas.1016071107 [PubMed: 21106759]

Dai P, Akimaru H, Tanaka Y, Maekawa T, Nakafuku M, Ishii S, 1999. Sonic Hedgehog-induced Activation of the Gli1Promoter Is Mediated by GLI3. J. Biol. Chem. 274, 8143–8152. [PubMed: 10075717]

Datto MB, Frederick JP, Pan L, Borton AJ, Zhuang Y, Wang X-F, 1999. Targeted Disruption of Smad3 Reveals an Essential Role in Transforming Growth Factor β-Mediated Signal Transduction. Mol. Cell. Biol. 19, 2495–2504. 10.1128/MCB.19.4.2495/ASSET/4EC3BE3F-943D-47F5-A009-FD1618AFC0C3/ASSETS/GRAPHIC/MB0491501007.JPEG [PubMed: 10082515]

de Soysa TY, Ranade SS, Okawa S, Ravichandran S, Huang Y, Salunga HT, Schricker A, del Sol A, Gifford CA, Srivastava D, 2019. Single-cell analysis of cardiogenesis reveals basis for organ-level developmental defects. Nature 572, 120–124. 10.1038/s41586-019-1414-x [PubMed: 31341279]

Delile J, Rayon T, Melchionda M, Edwards A, Briscoe J, Sagner A, 2019. Single cell transcriptomics reveals spatial and temporal dynamics of gene expression in the developing mouse spinal cord. Dev. Camb. 146. 10.1242/dev.173807

Dessaud E, McMahon AP, Briscoe J, 2008. Pattern formation in the vertebrate neural tube: A sonic hedgehog morphogen-regulated transcriptional network. Development. 10.1242/dev.009324

Dobin A, Davis CA, Schlesinger F, Drenkow J, Zaleski C, Jha S, Batut P, Chaisson M, Gingeras TR, 2013. STAR: Ultrafast universal RNA-seq aligner. Bioinformatics 29, 15–21. 10.1093/bioinformatics/bts635 [PubMed: 23104886]

Durand B, Raff M, 2000. A cell-intrinsic timer that operates during oligodendrocyte development. BioEssays 22, 64–71. 10.1002/(SICI)1521-1878(200001)22:1<64::AID-BIES11>3.0.CO;2-Q [PubMed: 10649292]

Dyer LA, Kirby ML, 2009. Sonic hedgehog maintains proliferation in secondary heart field progenitors and is required for normal arterial pole formation. Dev. Biol. 330, 305–317. [PubMed: 19361493]

Ebisuya M, Briscoe J, 2018. What does time mean in development? Development 145, dev164368. 10.1242/dev.164368 [PubMed: 29945985]

Ericson J, Morton S, Kawakami A, Roelink H, Jessell TM, 1996. Two Critical Periods of Sonic Hedgehog Signaling Required for the Specification of Motor Neuron Identity. Cell 87, 661–673. 10.1016/S0092-8674(00)81386-0 [PubMed: 8929535]

Friedland-Little JM, Hoffmann AD, Ocbina PJR, Peterson MA, Bosman JD, Chen Y, Cheng SY, Anderson KV, Moskowitz IP, 2011. A novel murine allele of Intraflagellar Transport Protein 172 causes a syndrome including VACTERL-like features with hydrocephalus. hmg.oxfordjournals.org.

Fuccillo M, Joyner AL, Fishell G, 2006. Morphogen to mitogen: the multiple roles of hedgehog signalling in vertebrate neural development. Nat. Rev. Neurosci. 2006 710 7, 772–783. 10.1038/nrn1990

Fujii M, Sakaguchi A, Kamata R, Nagao M, Kikuchi Y, Evans SM, Yoshizumi M, Shimono A, Saga Y, Kokubo H, 2017. Sfrp5 identifies murine cardiac progenitors for all myocardial structures except for the right ventricle. Nat. Commun. 8, 1–9. 10.1038/ncomms14664 [PubMed: 28232747]

Gascard P, Bilenky M, Sigaroudinia M, Zhao J, Li L, Carles A, Delaney A, Tam A, Kamoh B, Cho S, Griffith M, Chu A, Robertson G, Cheung D, Li I, Heravi-Moussavi A, Moksa M, Mingay M, Hussainkhel A, Davis B, Nagarajan RP, Hong C, Echipare L, O'Geen H, Hangauer MJ, Cheng JB, Neel D, Hu D, McManus MT, Moore R, Mungall A, Ma Y, Plettner P, Ziv E, Wang T, Farnham PJ, Jones SJM, Marra MA, Tlsty TD, Costello JF, Hirst M, 2015. Epigenetic and transcriptional determinants of the human breast. Nat. Commun. 2015 61 6, 1–10. 10.1038/ncomms7351

Gentile A, Bensimon-Brito A, Priya R, Maischein HM, Piesker J, Guenther S, Gunawan F, Stainier DYR, 2021. The emt transcription factor snai1 maintains myocardial wall integrity by repressing intermediate filament gene expression. eLife 10. 10.7554/ELIFE.66143

Gitler AD, Lu MM, Epstein JA, 2004. PlexinD1 and Semaphorin Signaling Are Required in Endothelial Cells for Cardiovascular Development. Dev. Cell 7, 107–116. 10.1016/J.DEVCEL.2004.06.002 [PubMed: 15239958]

Goddeeris MM, Rho S, Petiet A, Davenport CL, Johnson GA, Meyers EN, Klingensmith J, 2008. Intracardiac septation requires hedgehog-dependent cellular contributions from outside the heart. Development 135, 1887–1895. [PubMed: 18441277]

Goddeeris MM, Schwartz R, Klingensmith J, Meyers EN, 2007. Independent requirements for Hedgehog signaling by both the anterior heart field and neural crest cells for outflow tract development. Development 134, 1593–1604. [PubMed: 17344228]

Gomez C, Özbudak EM, Wunderlich J, Baumann D, Lewis J, Pourquié O, 2008. Control of segment number in vertebrate embryos. Nature 454, 335–339. [PubMed: 18563087]

Gu C, Yoshida Y, Livet J, Reimert DV, Mann F, Merte J, Henderson CE, Jessell TM, Kolodkin AL, Ginty DD, 2005. Semaphorin 3E and plexin-D1 control vascular pattern independently of neuropilins. Science 307, 265–268. 10.1126/SCIENCE.1105416/SUPPL_FILE/GU.SOM.PDF [PubMed: 15550623]

Gu Z, Eils R, Schlesner M, 2016. Complex heatmaps reveal patterns and correlations in multidimensional genomic data. Bioinformatics 32, 2847–2849. 10.1093/bioinformatics/btw313 [PubMed: 27207943]

Haghverdi L, Büttner M, Wolf FA, Buettner F, Theis FJ, 2016. Diffusion pseudotime robustly reconstructs lineage branching. Nat. Methods 13, 845–848. 10.1038/nmeth.3971 [PubMed: 27571553]

Han L, Chaturvedi P, Kishimoto K, Koike H, Nasr T, Iwasawa K, Giesbrecht K, Witcher PC, Eicher A, Haines L, Lee Y, Shannon JM, Morimoto M, Wells JM, Takebe T, Zorn AM, 2020. Single cell transcriptomics identifies a signaling network coordinating endoderm and mesoderm diversification during foregut organogenesis. Nat. Commun. 2020 111 11, 1–16. 10.1038/s41467-020-17968-x

Han L, Koike H, Chaturvedi P, Kishimoto K, Iwasawa K, Giesbrecht K, Witcher P, Eicher A, Nasr T, Haines L, Shannon J, Morimoto M, Wells J, Takebe T, Zorn A, 2019. Single cell transcriptomics reveals a signaling roadmap coordinating endoderm and mesoderm lineage diversification during foregut organogenesis. bioRxiv 756825. 10.1101/756825

Hao Y, Hao S, Andersen-Nissen E, Mauck WM, Zheng S, Butler A, Lee MJ, Wilk AJ, Darby C, Zager M, Hoffman P, Stoeckius M, Papalexi E, Mimitou EP, Jain J, Srivastava A, Stuart T, Fleming LM, Yeung B, Rogers AJ, McElrath JM, Blish CA, Gottardo R, Smibert P, Satija R, 2021. Integrated analysis of multimodal single-cell data. Cell 184, 3573–3587.e29. 10.1016/J.CELL.2021.04.048 [PubMed: 34062119]

Harima Y, Takashima Y, Ueda Y, Ohtsuka T, Kageyama R, 2013. Accelerating the Tempo of the Segmentation Clock by Reducing the Number of Introns in the Hes7 Gene. Cell Rep. 3, 1–7. 10.1016/j.celrep.2012.11.012 [PubMed: 23219549]

Hasenpusch-Theil K, West S, Kelman A, Kozic Z, Horrocks S, McMahon AP, Price DJ, Mason JO, Theil T, 2018. Gli3 controls the onset of cortical neurogenesis by regulating the radial glial cell cycle through Cdk6 expression. Dev. Camb. 145. 10.1242/dev.163147

Heinz S, Benner C, Spann N, Bertolino E, Lin YC, Laslo P, Cheng JX, Murre C, Singh H, Glass CK, 2010. Simple Combinations of Lineage-Determining Transcription Factors Prime cis-Regulatory Elements Required for Macrophage and B Cell Identities. Mol. Cell 38, 576–589. 10.1016/j.molcel.2010.05.004 [PubMed: 20513432]

Herzog VA, Reichholf B, Neumann T, Rescheneder P, Bhat P, Burkard TR, Wlotzka W, Von Haeseler A, Zuber J, Ameres SL, 2017. Thiol-linked alkylation of RNA to assess expression dynamics. Nat. Methods 2017 1412 14, 1198–1204. 10.1038/nmeth.4435

Hoffmann AD, Peterson MA, Friedland-Little JM, Anderson SA, Moskowitz IP, 2009. sonic hedgehog is required in pulmonary endoderm for atrial septation. Development 136, 1761–1770. [PubMed: 19369393]

Hoffmann AD, Yang XH, Burnicka-Turek O, Bosman JD, Ren X, Steimle JD, Vokes SA, McMahon AP, Kalinichenko VV, Moskowitz IP, 2014. PLOS Genetics: Foxf Genes Integrate Tbx5 and Hedgehog Pathways in the Second Heart Field for Cardiac Septation. journals.plos.org 10, e1004604.

Hooper JE, Scott MP, 2005. Communicating with Hedgehogs. Nat. Rev. Mol. Cell Biol. 6, 306–317. 10.1038/nrm1622 [PubMed: 15803137]

Hoshiba Y, Toda T, Ebisu H, Wakimoto M, Yanagi S, Kawasaki H, 2016. Sox11 Balances Dendritic Morphogenesis with Neuronal Migration in the Developing Cerebral Cortex. J. Neurosci. 36, 5775–5784. 10.1523/JNEUROSCI.3250-15.2016 [PubMed: 27225767]

Hu MC, Mo R, Bhella S, Wilson CW, Chuang PT, Hui CC, Rosenblum ND, 2006. GLI3-dependent transcriptional repression of Gli1, Gli2 and kidney patterning genes disrupts renal morphogenesis. Development 133, 569–578. 10.1242/dev.02220 [PubMed: 16396903]

Huangfu D, Liu A, Rakeman AS, Murcia NS, Niswander L, Anderson KV, 2003. Hedgehog signalling in the mouse requires intraflagellar transport proteins. Nature 426, 83–87. 10.1038/nature02061 [PubMed: 14603322]

Hubaud A, Pourquié O, 2014. Signalling dynamics in vertebrate segmentation. Nat. Rev. Mol. Cell Biol. 10.1038/nrm3891

Hui C, Angers S, 2011. Gli Proteins in Development and Disease. Annu. Rev. Cell Dev. Biol. 27, 513–537. 10.1146/annurev-cellbio-092910-154048 [PubMed: 21801010]

Hutson MR, Zeng XL, Kim AJ, Antoon E, Harward S, Kirby ML, 2010. Arterial pole progenitors interpret opposing FGF/BMP signals to proliferate or differentiate. Development 137, 3001–3011. 10.1242/dev.051565 [PubMed: 20702561]

Iacovino M, Bosnakovski D, Fey H, Rux D, Bajwa G, Mahen E, Mitanoska A, Xu Z, Kyba M, 2011. Inducible Cassette Exchange: A Rapid and Efficient System Enabling Conditional Gene Expression in Embryonic Stem and Primary Cells. STEM CELLS 29, 1580–1588. 10.1002/stem.715 [PubMed: 22039605]

Ikegami K, Secchia S, Almakki O, Lieb JD, Moskowitz IP, 2020. Phosphorylated Lamin A/C in the Nuclear Interior Binds Active Enhancers Associated with Abnormal Transcription in Progeria. Dev. Cell 52, 699–713.e11. 10.1016/J.DEVCEL.2020.02.011 [PubMed: 32208162]

Imayoshi I, Isomura A, Harima Y, Kawaguchi K, Kori H, Miyachi H, Fujiwara T, Ishidate F, Kageyama R, 2013. Oscillatory control of factors determining multipotency and fate in mouse neural progenitors. Science 342, 1203–1208. 10.1126/science.1242366 [PubMed: 24179156]

Ingham PW, Placzek M, 2006. Orchestrating ontogenesis: variations on a theme by sonic hedgehog. Nat. Rev. Genet. 7, 841–850. 10.1038/nrg1969 [PubMed: 17047684]

Inoue J, Ueda Y, Bando T, Mito T, Noji S, Ohuchi H, 2013. The expression of LIM-homeobox genes, Lhx1 and Lhx5, in the forebrain is essential for neural retina differentiation. Dev. Growth Differ. 55, 668–675. 10.1111/DGD.12074 [PubMed: 24024588]

Jagani Z, Mora-Blanco EL, Sansam CG, McKenna ES, Wilson B, Chen D, Klekota J, Tamayo P, Nguyen PTL, Tolstorukov M, Park PJ, Cho Y-J, Hsiao K, Buonamici S, Pomeroy SL, Mesirov JP, Ruffner H, Bouwmeester T, Luchansky SJ, Murtie J, Kelleher JF, Warmuth M, Sellers WR, Roberts CWM, Dorsch M, 2010. Loss of the tumor suppressor Snf5 leads to aberrant activation of the Hedgehog-Gli pathway. Nat. Med. 16, 1429–1433. [PubMed: 21076395]

Jain R, Li D, Gupta M, Manderfield LJ, Ifkovits JL, Wang Q, Liu F, Liu Y, Poleshko A, Padmanabhan A, Raum JC, Li L, Morrisey EE, Lu MM, Won KJ, Epstein JA, 2015. Integration of Bmp and Wnt signaling by Hopx specifies commitment of cardiomyoblasts. Science 348, aaa6071–aaa6071. [PubMed: 26113728]

Jarrar W, Dias JM, Ericson J, Arnold HH, Holz A, 2015. Nkx2.2 and Nkx2.9 Are the Key Regulators to Determine Cell Fate of Branchial and Visceral Motor Neurons in Caudal Hindbrain. PLOS ONE 10, e0124408. 10.1371/JOURNAL.PONE.0124408 [PubMed: 25919494]

Jeon S, Seong RH, 2016. Anteroposterior Limb Skeletal Patterning Requires the Bifunctional Action of SWI/SNF Chromatin Remodeling Complex in Hedgehog Pathway. PLoS Genet. 12, e1005915. [PubMed: 26959361]

Jepsen K, Hermanson O, Onami TM, Gleiberman AS, Lunyak V, McEvilly RJ, Kurokawa R, Kumar V, Liu F, Seto E, Hedrick SM, Mandel G, Glass CK, Rose DW, Rosenfeld MG, 2000. Combinatorial Roles of the Nuclear Receptor Corepressor in Transcription and Development. Cell 102, 753–763. 10.1016/S0092-8674(00)00064-7 [PubMed: 11030619]

Jessell TM, 2000. Neuronal specification in the spinal cord:inductive signals and transcriptional codes. Nat. Rev. Genet. 1, 20–29. [PubMed: 11262869]

Jiang J, Hui C-C, 2008. Hedgehog signaling in development and cancer. Dev. Cell 15, 801–12. 10.1016/j.devcel.2008.11.010 [PubMed: 19081070]

John S, Sabo PJ, Thurman RE, Sung MH, Biddie SC, Johnson TA, Hager GL, Stamatoyannopoulos JA, 2011. Chromatin accessibility pre-determines glucocorticoid receptor binding patterns. Nat. Genet. 2011 433 43, 264–268. 10.1038/ng.759

Kitamura K, M. H, Miyagawa-Tomita S, Yanazawa M, Katoh-Fukui Y, Suzuki R, Ohuchi H, Suehiro A, Motegi Y, Nakahara Y, Kondo S, Yokoyama M, 1999. Mouse Pitx2 deficiency leads to anomalies of the ventral body wall, heart, extra- and periocular mesoderm and right pulmonary isomerism | Development. Development 5749–5758. [PubMed: 10572050]

Kaldis P, Richardson HE, 2012. When cell cycle meets development. Development. 10.1242/dev.073288

Karhadkar SS, Steven Bova G, Abdallah N, Dhara S, Gardner D, Maitra A, Isaacs JT, Berman DM, Beachy PA, 2004. Hedgehog signalling in prostate regeneration, neoplasia and metastasis. Nature 431, 707–712. 10.1038/nature02962 [PubMed: 15361885]

Kattman SJ, Witty AD, Gagliardi M, Dubois NC, Niapour M, Hotta A, Ellis J, Keller G, 2011. Stage-Specific Optimization of Activin/Nodal and BMP Signaling Promotes Cardiac Differentiation of Mouse and Human Pluripotent Stem Cell Lines. Cell Stem Cell 8, 228–240. [PubMed: 21295278]

Kawagishi H, Xiong J, Rovira II, Pan H, Yan Y, Fleischmann BK, Yamada M, Finkel T, 2018. Sonic hedgehog signaling regulates the mammalian cardiac regenerative response. J. Mol. Cell. Cardiol. 123, 180–184. 10.1016/j.yjmcc.2018.09.005 [PubMed: 30236923]

Kelly RG, 2012. The second heart field. Curr. Top. Dev. Biol. 100, 33–65. [PubMed: 22449840]

Kelly RG, Brown NA, Buckingham ME, 2001. The Arterial Pole of the Mouse Heart Forms from Fgf10-Expressing Cells in Pharyngeal Mesoderm. Dev. Cell 1, 435–440. [PubMed: 11702954]

Kelly RG, Buckingham ME, Moorman AF, 2014. Heart fields and cardiac morphogenesis. Cold Spring Harb. Perspect. Med. 4, a015750. 10.1101/cshperspect.a015750 [PubMed: 25274757]

Kent WJ, Sugnet CW, Furey TS, Roskin KM, Pringle TH, Zahler AM, Haussler a. D., 2002. The Human Genome Browser at UCSC. Genome Res. 12, 996–1006. 10.1101/gr.229102 [PubMed: 12045153]

Kohwi M, Doe CQ, 2013. Temporal fate specification and neural progenitor competence during development. Nat. Rev. Neurosci. 14, 823–838. 10.1038/nrn3618 [PubMed: 24400340]

Kothary R, Clapoff S, Darling S, Perry MD, Moran LA, Rossant J, 1989. Inducible expression of an hsp68-lacZ hybrid gene in transgenic mice. Development 105, 707–714. [PubMed: 2557196]

Kutejova E, Sasai N, Shah A, Gouti M, Briscoe J, 2016. Neural Progenitors Adopt Specific Identities by Directly Repressing All Alternative Progenitor Transcriptional Programs. Dev. Cell 36, 639–653. [PubMed: 26972603]

Langmead B, Salzberg SL, 2012. Fast gapped-read alignment with Bowtie 2. Nat. Methods 9, 357–359. 10.1038/nmeth.1923 [PubMed: 22388286]

Lanier J, Dykes IM, Nissen S, Eng SR, Turner EE, 2009. Brn3a regulates the transition from neurogenesis to terminal differentiation and represses non-neural gene expression in the trigeminal ganglion. Dev. Dyn. 238, 3065–3079. 10.1002/DVDY.22145 [PubMed: 19877281]

Lee J, Platt KA, Censullo P, Ruiz i Altaba A, 1997. Gli1 is a target of Sonic hedgehog that induces ventral neural tube development. Development 124, 2537–2552. [PubMed: 9216996]

Lee RTH, Zhao Z, Ingham PW, 2016. Hedgehog signalling. Dev. Camb. Engl. 143, 367–72. 10.1242/dev.120154

Lei Q, Jeong Y, Misra K, Li S, Zelman AK, Epstein DJ, Matise MP, 2006. Wnt Signaling Inhibitors Regulate the Transcriptional Response to Morphogenetic Shh-Gli Signaling in the Neural Tube. Dev. Cell 11, 325–337. 10.1016/j.devcel.2006.06.013 [PubMed: 16950124]

Lescroart F, Chabab S, Lin X, Rulands S, Paulissen C, Rodolosse A, Auer H, Achouri Y, Dubois C, Bondue A, Simons BD, Blanpain C, 2014. Early lineage restriction in temporally distinct populations of Mesp1 progenitors during mammalian heart development. Nat. Cell Biol. 16, 829–840. [PubMed: 25150979]

Lex RK, Ji Z, Falkenstein KN, Zhou W, Henry JL, Ji H, Vokes SA, 2020. GLI transcriptional repression regulates tissue-specific enhancer activity in response to hedgehog signaling. eLife 9, 1–24. 10.7554/eLife.50670

Li CF, Chen JY, Ho YH, Hsu WH, Wu LC, Lan HY, Hsu DSS, Tai SK, Chang YC, Yang MH, 2019. Snail-induced claudin-11 prompts collective migration for tumour progression. Nat. Cell Biol. 2019 212 21, 251–262. 10.1038/s41556-018-0268-z

Li P, Pashmforoush M, Sucov HM, 2010. Retinoic Acid Regulates Differentiation of the Secondary Heart Field and TGFβ-Mediated Outflow Tract Septation. Dev. Cell 18, 480–485. 10.1016/j.devcel.2009.12.019 [PubMed: 20230754]

Lister R, Pelizzola M, Dowen RH, Hawkins RD, Hon G, Tonti-Filippini J, Nery JR, Lee L, Ye Z, Ngo QM, Edsall L, Antosiewicz-Bourget J, Stewart R, Ruotti V, Millar AH, Thomson JA, Ren B, Ecker JR, 2009. Human DNA methylomes at base resolution show widespread epigenomic differences. Nat. 2009 4627271 462, 315–322. 10.1038/nature08514

Liu C, Wang M, Wei X, Wu L, Xu J, Dai X, Xia J, Cheng M, Yuan Y, Zhang P, Li J, Feng T, Chen A, Zhang W, Chen F, Shang Z, Zhang X, Peters BA, Liu L, 2019. An ATAC-seq atlas of chromatin accessibility in mouse tissues. Sci. Data 2019 61 6, 1–10. 10.1038/s41597-019-0071-0

Liu JA, Ngan ES-W, 2014. Hedgehog and Notch Signaling in Enteric Nervous System Development. Neurosignals 22, 1–13. 10.1159/000356305 [PubMed: 24356576]

Lu J, Richardson JA, Olson EN, 1998. Capsulin: A novel bHLH transcription factor expressed in epicardial progenitors and mesenchyme of visceral organs. Mech. Dev. 73, 23–32. 10.1016/S0925-4773(98)00030-6 [PubMed: 9545521]

Macosko EZ, Basu A, Satija R, Nemesh J, Shekhar K, Goldman M, Tirosh I, Bialas AR, Kamitaki N, Martersteck EM, Trombetta JJ, Weitz DA, Sanes JR, Shalek AK, Regev A, McCarroll SA, 2015. Highly Parallel Genome-wide Expression Profiling of Individual Cells Using Nanoliter Droplets. Cell 161, 1202–1214. [PubMed: 26000488]

Magnani L, Ballantyne EB, Zhang X, Lupien M, 2011. PBX1 Genomic Pioneer Function Drives ERα Signaling Underlying Progression in Breast Cancer. PLOS Genet. 7, e1002368. 10.1371/JOURNAL.PGEN.1002368 [PubMed: 22125492]

Malatesta M, Steinhauer C, Mohammad F, Pandey DP, Squatrito M, Helin K, 2013. Histone acetyltransferase PCAF is required for hedgehog-Gli-dependent transcription and cancer cell proliferation. Cancer Res. 73, 6323–6333. 10.1158/0008-5472.CAN-12-4660 [PubMed: 23943798]

Robinson Mark D., M DJ.S GK, 2010. edgeR: a Bioconductor package for differential expression analysis of digital gene expression data | Bioinformatics | Oxford Academic. Bioinformatics 26, 139–140. [PubMed: 19910308]

Marler KJM, Becker-Barroso E, Martínez A, Llovera M, Wentzel C, Poopalasundaram S, Hindges R, Soriano E, Comella J, Drescher U, 2008. A TrkB/EphrinA Interaction Controls Retinal Axon Branching and Synaptogenesis. J. Neurosci. 28, 12700–12712. 10.1523/JNEUROSCI.1915-08.2008 [PubMed: 19036963]

Mazzà D, Infante P, Colicchia V, Greco A, Alfonsi R, Siler M, Antonucci L, Po A, De Smaele E, Ferretti E, Capalbo C, Bellavia D, Canettieri G, Giannini G, Screpanti I, Gulino A, Di Marcotullio L, 2013. PCAF ubiquitin ligase activity inhibits Hedgehog/Gli1 signaling in p53-dependent response to genotoxic stress. Cell Death Differ. 2013 2012 20, 1688–1697. 10.1038/cdd.2013.120

McEvilly RJ, Erkman L, Luo L, Sawchenko PE, Ryan AF, Rosenfeld MG, 1996. Requirement for Brn-3.0 in differentiation and survival of sensory and motor neurons. Nat. 1996 3846609 384, 574–577. 10.1038/384574a0

McMahon AP, Ingham PW, Tabin CJ, 2003. 1 Developmental roles and clinical significance of Hedgehog signaling. Curr. Top. Dev. Biol. 10.1016/s0070-2153(03)53002-2

Meilhac SM, Esner M, Kelly RG, Nicolas JF, Buckingham ME, 2004. The clonal origin of myocardial cells in different regions of the embryonic mouse heart. Dev. Cell 6, 685–698. 10.1016/S1534-5807(04)00133-9 [PubMed: 15130493]

Miyaji T, Nakase T, Iwasaki M, Kuriyama K, Tamai N, Higuchi C, Myoui A, Tomita T, Yoshikawa H, 2003. Expression and distribution of transcripts for sonic hedgehog in the early phase of fracture repair. Histochem. Cell Biol. 119, 233–237. 10.1007/s00418-003-0501-z [PubMed: 12649738]

Momen-Roknabadi A, Di Talia S, Wieschaus E, 2016. Transcriptional Timers Regulating Mitosis in Early Drosophila Embryos. Cell Rep. 16, 2793–2801. 10.1016/j.celrep.2016.08.034 [PubMed: 27626650]

Moss EG, 2007. Heterochronic Genes and the Nature of Developmental Time. Curr. Biol. 17, R425–R434. 10.1016/j.cub.2007.03.043 [PubMed: 17550772]

Mugford JW, Sipilae P, McMahon JA, McMahon AP, 2008. Osr1 expression demarcates a multi-potent population of intermediate mesoderm that undergoes progressive restriction to an Osr1-dependent nephron progenitor compartment within the mammalian kidney. Dev. Biol. 324, 88–98. [PubMed: 18835385]

Mukherjee S, Chaturvedi P, Rankin SA, Fish MB, Wlizla M, Paraiso KD, MacDonald M, Chen X, Weirauch MT, Blitz IL, Cho KW, Zorn AM, 2020. Sox17 and β-catenin co-occupy Wnt-responsive enhancers to govern the endoderm gene regulatory network. eLife 9. 10.7554/eLife.58029

Mullen AC, Orlando DA, Newman JJ, Lovén J, Kumar RM, Bilodeau S, Reddy J, Guenther MG, DeKoter RP, Young RA, 2011. Master Transcription Factors Determine Cell-Type-Specific Responses to TGF-β Signaling. Cell 147, 565–576. [PubMed: 22036565]

Neeb Z, Lajiness JD, Bolanis E, Conway SJ, 2013. Cardiac outflow tract anomalies. Wiley Interdiscip. Rev. Dev. Biol. 2, 499–530. 10.1002/wdev.98 [PubMed: 24014420]

Ng JMY, Curran T, 2011. The Hedgehog's tale: Developing strategies for targeting cancer. Nat. Rev. Cancer. 10.1038/nrc3079

Ngan ES-W, Kim K-H, Hui C. -c., 2012. Sonic Hedgehog Signaling and VACTERL Association. Mol. Syndromol. 4, 32–45. 10.1159/000345725

Nieuwenhuis E, Hui CC, 2005. Hedgehog signaling and congenital malformations. Clin. Genet. 10.1111/j.1399-0004.2004.00360.x

Nik AM, Johansson JA, Ghiami M, Reyahi A, Carlsson P, 2016. Foxf2 is required for secondary palate development and Tgfβ signaling in palatal shelf mesenchyme. Dev. Biol. 415, 14–23. 10.1016/J.YDBIO.2016.05.013 [PubMed: 27180663]

Nye MD, Almada LL, Fernandez-Barrena MG, Marks DL, Elsawa SF, Vrabel A, Tolosa EJ, Ellenrieder V, Fernandez-Zapico ME, 2014. The Transcription Factor GLI1 Interacts with SMAD Proteins to Modulate Transforming Growth Factor β-Induced Gene Expression in a p300/CREB-binding Protein-associated Factor (PCAF)-dependent Manner. J. Biol. Chem. 289, 15495–15506. 10.1074/JBC.M113.545194 [PubMed: 24739390]

Ocbina PJR, Eggenschwiler JT, Moskowitz I, Anderson KV, 2011. Complex interactions between genes controlling trafficking in primary cilia. Nat. Genet. 43, 547–553. 10.1038/ng.832 [PubMed: 21552265]

Ochoa B, Syn WK, Delgado I, Karaca GF, Jung Y, Wang J, Zubiaga AM, Fresnedo O, Omenetti A, Zdanowicz M, Choi SS, Diehl AM, 2010. Hedgehog signaling is critical for normal liver regeneration after partial hepatectomy in mice. Hepatology 51, 1712–1723. 10.1002/hep.23525 [PubMed: 20432255]

Oosterveen T, Kurdija S, Alekseenko Z, Uhde CW, Bergsland M, Sandberg M, Andersson E, Dias JM, Muhr J, Ericson J, 2012. Mechanistic differences in the transcriptional interpretation of local and long-range Shh morphogen signaling. Dev. Cell 23, 1006–19. 10.1016/j.devcel.2012.09.015 [PubMed: 23153497]

Otani T, Marchetto MC, Gage FH, Simons BD, Livesey FJ, 2016. 2D and 3D Stem Cell Models of Primate Cortical Development Identify Species-Specific Differences in Progenitor Behavior Contributing to Brain Size. Cell Stem Cell 18, 467–480. 10.1016/j.stem.2016.03.003 [PubMed: 27049876]

Ozanna Burnicka-Turek Jeffrey D. Steimle, Huang Wenhui, Felker Lindsay, Kamp Anna, Kweon Junghun, Peterson Michael, Reeves Roger H., Maslen Cheryl L., Gruber Peter J., Yang Xinan H., Shendure Jay, Moskowitz Ivan P., 2016. Cilia gene mutations cause atrioventricular septal defects by multiple mechanisms | Human Molecular Genetics | Oxford Academic. Hum. Mol. Genet. 25, 3011–3028. [PubMed: 27340223]

Pabst O, Rummelies J, Winter B, Arnold HH, 2003. Targeted disruption of the homeobox gene Nkx2.9 reveals a role in development of the spinal accessory nerve. Development 130, 1193–1202. 10.1242/DEV.00346 [PubMed: 12571110]

Paul MH, Harvey RP, Wegner M, Sock E, 2014. Cardiac outflow tract development relies on the complex function of Sox4 and Sox11 in multiple cell types. Cell. Mol. Life Sci. 71, 2931–2945. 10.1007/S00018-013-1523-X/FIGURES/8 [PubMed: 24310815]

Pearson BJ, Doe CQ, 2004. SPECIFICATION OF TEMPORAL IDENTITY IN THE DEVELOPING NERVOUS SYSTEM. Annu. Rev. Cell Dev. Biol. 20, 619–647. 10.1146/annurev.cellbio.19.111301.115142 [PubMed: 15473854]

Peng T, Frank DB, Kadzik RS, Morley MP, Rathi KS, Wang T, Zhou S, Cheng L, Lu MM, Morrisey EE, 2015. Hedgehog actively maintains adult lung quiescence and regulates repair and regeneration. Nature 526, 578–582. [PubMed: 26436454]

Peng T, Tian Y, Boogerd CJ, Lu MM, Kadzik RS, Stewart KM, Evans SM, Morrisey EE, 2013. Coordination of heart and lung co-development by a multipotent cardiopulmonary progenitor. Nature 500, 589–592. [PubMed: 23873040]

Peterson KA, Nishi Y, Ma W, Vedenko A, Shokri L, Zhang X, McFarlane M, Baizabal JM, Junker JP, van Oudenaarden A, Mikkelsen T, Bernstein BE, Bailey TL, Bulyk ML, Wong WH, McMahon AP, 2012. Neural-specific Sox2 input and differential Gli-binding affinity provide context and positional information in Shh-directed neural patterning. Genes Dev. 26, 2802–2816. 10.1101/gad.207142.112 [PubMed: 23249739]

Petrova R, Joyner AL, 2014. Roles for Hedgehog signaling in adult organ homeostasis and repair. Development 141, 3445–3457. [PubMed: 25183867]

Pourquié O, 1998. Clocks regulating developmental processes. Curr. Opin. Neurobiol. 8, 665–670. 10.1016/S0959-4388(98)80097-4 [PubMed: 9811632]

Quinlan AR, Hall I, 2010. BEDTools: a flexible suite of utilities for comparing genomic features | Bioinformatics | Oxford Academic. Bioinformatics 26, 841–842. [PubMed: 20110278]

Rankin SA, Steimle JD, Yang XH, Rydeen AB, Agarwal K, Chaturvedi P, Ikegami K, Herriges MJ, Moskowitz IP, Zorn AM, 2021. Tbx5 drives aldh1a2 expression to regulate a ra-hedgehog-wnt gene regulatory network coordinating cardiopulmonary development. eLife 10. 10.7554/ELIFE.69288

Reinhardt R, Gullotta F, Nusspaumer G, Ünal E, Ivanek R, Zuniga A, Zeller R, 2019. Molecular signatures identify immature mesenchymal progenitors in early mouse limb buds that respond differentially to morphogen signaling. Dev. Camb. 146. 10.1242/dev.173328

Robb L, Mifsud L, Hartley L, Biben C, Copeland NG, Gilbert DJ, Jenkins NA, Harvey RP, 1998. epicardin: A novel basic helix-loop-helix transcription factor gene expressed in epicardium, branchial arch myoblasts, and mesenchyme of developing lung, gut, kidney, and gonads. Dev. Dyn. 213, 105–113. 10.1002/(SICI)1097-0177(199809)213:1<105::AID-AJA10>3.0.CO;2-1 [PubMed: 9733105]

Rochais F, Mesbah K, Kelly RG, 2009. Signaling Pathways Controlling Second Heart Field Development. Circ. Res. 104, 933–942. [PubMed: 19390062]

Roy S, Ingham PW, 2002. Hedgehogs tryst with the cell cycle. J. Cell Sci. 10.1242/jcs.00158

Ruiz i Altaba A, Mas C, Stecca B, 2007. The Gli code: an information nexus regulating cell fate, stemness and cancer. Trends Cell Biol. 17, 438–447. 10.1016/J.TCB.2007.06.007 [PubMed: 17845852]

Ruiz i Altaba A, Sánchez P, Dahmane N, 2002. Gli and hedgehog in cancer: Tumours, embryos and stem cells. Nat. Rev. Cancer. 10.1038/nrc796

Sakurai A, Gavard J, Annas-Linhares Y, Basile JR, Amornphimoltham P, Palmby TR, Yagi H, Zhang F, Randazzo PA, Li X, Weigert R, Gutkind JS, 2010. Semaphorin 3E Initiates Antiangiogenic Signaling through Plexin D1 by Regulating Arf6 and R-Ras. Mol. Cell. Biol. 30, 3086–3098. 10.1128/MCB.01652-09/SUPPL_FILE/SAKURAI_MOVIE_S2.MOV [PubMed: 20385769]

Sasai N, Kutejova E, Briscoe J, 2014. Integration of Signals along Orthogonal Axes of the Vertebrate Neural Tube Controls Progenitor Competence and Increases Cell Diversity. PLoS Biol. 12, e1001907. 10.1371/journal.pbio.1001907 [PubMed: 25026549]

Sasaki H, Hui C, Nakafuku M, Kondoh H, Michaud J, Heng HH-Q, Chik KW, Shi X-M, Tsui L-C, Cheng SH, Joyner AL, Hui C-C, 1997. A binding site for Gli proteins is essential for HNF-3beta floor plate enhancer activity in transgenics and can respond to Shh in vitro. Dev. Camb. Engl. 124, 1313–22.

Schneider CA, Rasband WS, Eliceiri KW, 2012. NIH Image to ImageJ: 25 years of image analysis. Nat. Methods 9, 671–675. [PubMed: 22930834]

Selewa A, Dohn R, Eckart H, Lozano S, Xie B, Gauchat E, Elorbany R, Rhodes K, Burnett J, Gilad Y, Pott S, Basu A, 2020. Systematic Comparison of High-throughput Single-Cell and Single-Nucleus Transcriptomes during Cardiomyocyte Differentiation. Sci. Rep. 10, 1–13. 10.1038/s41598-020-58327-6 [PubMed: 31913322]

Shi X, Wang Q, Gu J, Xuan Z, Wu JI, 2016. SMARCA4/Brg1 coordinates genetic and epigenetic networks underlying Shh-type medulloblastoma development. Oncogene 35, 5746–5758. 10.1038/onc.2016.108 [PubMed: 27065321]

Shi X, Zhang Z, Zhan X, Cao M, Satoh T, Akira S, Shpargel K, Magnuson T, Li Q, Wang R, Wang C, Ge K, Wu J, 2014. An epigenetic switch induced by Shh signalling regulates gene activation during development and medulloblastoma growth. Nat. Commun. 5, 1–12. 10.1038/ncomms6425

Shin K, Lee J, Guo N, Kim J, Lim A, Qu L, Mysorekar IU, Beachy PA, 2011. Hedgehog/Wnt feedback supports regenerative proliferation of epithelial stem cells in bladder. Nature 472, 110–114. 10.1038/nature09851 [PubMed: 21389986]

Singh BN, Koyano-Nakagawa N, Gong W, Moskowitz IP, Weaver CV, Braunlin E, Das S, van Berlo JH, Garry MG, Garry DJ, 2018. A conserved HH-Gli1-Mycn network regulates heart regeneration from newt to human. Nat. Commun. 9, 4237. 10.1038/s41467-018-06617-z [PubMed: 30315164]

Smith KK, 2003. Time's arrow: Heterochrony and the evolution of development. Int. J. Dev. Biol. 10.1387/ijdb.14756337

Snarr BS, Wirrig EE, Phelps AL, Trusk TC, Wessels A, 2007. A spatiotemporal evaluation of the contribution of the dorsal mesenchymal protrusion to cardiac development. Dev. Dyn. 236, 1287–1294. [PubMed: 17265457]

Sun JX, Chang TF, Li MH, Sun LJ, Yan XC, Yang ZY, Liu Y, Xu WQ, Lv Y, Su JB, Liang L, Han H, Dou GR, Wang YS, 2018. SNAI1, an endothelial–mesenchymal transition transcription factor, promotes the early phase of ocular neovascularization. Angiogenesis 21, 635–652. 10.1007/S10456-018-9614-9/FIGURES/8 [PubMed: 29675549]

Suter TACS, Blagburn SV, Fisher SE, Anderson-Keightly HM, D'Elia KP, Jaworski A, 2020. TAG-1 Multifunctionality Coordinates Neuronal Migration, Axon Guidance, and Fasciculation. Cell Rep. 30, 1164–1177.e7. 10.1016/J.CELREP.2019.12.085 [PubMed: 31995756]

Suzuki R, Shimodaira H, 2006. Pvclust: an R package for assessing the uncertainty in hierarchical clustering. Bioinformatics 22, 1540–1542. 10.1093/BIOINFORMATICS/BTL117 [PubMed: 16595560]

Taipale J, Beachy PA, 2001. The Hedgehog and Wnt signalling pathways in cancer. Nature. 10.1038/35077219

Tan SK, Lin ZH, Chang CW, Varang V, Chng KR, Pan YF, Yong EL, Sung WK, Cheung E, 2011. AP-2γ regulates oestrogen receptor-mediated long-range chromatin interaction and gene transcription. EMBO J. 30, 2569–2581. 10.1038/EMBOJ.2011.151 [PubMed: 21572391]

Tchorz JS, Tome M, Cloëtta D, Sivasankaran B, Grzmil M, Huber RM, Rutz-Schatzmann F, Kirchhoff F, Schaeren-Wiemers N, Gassmann M, Hemmings BA, Merlo A, Bettler B, 2012. Constitutive Notch2 signaling in neural stem cells promotes tumorigenic features and astroglial lineage entry. Cell Death Dis. 2012 36 3, e325–e325. 10.1038/cddis.2012.65

Teglund S, Toftgård R, 2010. Hedgehog beyond medulloblastoma and basal cell carcinoma. Biochim. Biophys. Acta - Rev. Cancer. 10.1016/j.bbcan.2010.01.003

Tirosh I, Izar B, Prakadan SM, Wadsworth MH, Treacy D, Trombetta JJ, Rotem A, Rodman C, Lian C, Murphy G, Fallahi-Sichani M, Dutton-Regester K, Lin JR, Cohen O, Shah P, Lu D, Genshaft AS, Hughes TK, Ziegler CGK, Kazer SW, Gaillard A, Kolb KE, Villani AC, Johannessen CM, Andreev AY, Van Allen EM, Bertagnolli M, Sorger PK, Sullivan RJ, Flaherty KT, Frederick DT, Jané-Valbuena J, Yoon CH, Rozenblatt-Rosen O, Shalek AK, Regev A, Garraway LA, 2016. Dissecting the multicellular ecosystem of metastatic melanoma by single-cell RNA-seq. Science 352, 189–196. 10.1126/science.aad0501 [PubMed: 27124452]

Tirosh-Finkel L, Zeisel A, Brodt-Ivenshitz M, Shamai A, Yao Z, Seger R, Domany E, Tzahor E, 2010. BMP-mediated inhibition of FGF signaling promotes cardiomyocyte differentiation of anterior heart field progenitors. Development 137, 2989–3000. 10.1242/DEV.051649 [PubMed: 20702560]

Tomic D, Miller KP, Kenny HA, Woodruff TK, Hoyer P, Flaws JA, 2004. Ovarian Follicle Development Requires Smad3. Mol. Endocrinol. 18, 2224–2240. 10.1210/ME.2003-0414 [PubMed: 15192076]

Traag VA, Waltman L, van Eck NJ, 2019. From Louvain to Leiden: guaranteeing well-connected communities. Sci. Rep. 9, 1–12. 10.1038/s41598-019-41695-z [PubMed: 30626917]

Trapnell C, Hendrickson DG, Sauvageau M, Goff L, Rinn JL, Pachter L, 2013. Differential analysis of gene regulation at transcript resolution with RNA-seq. Nat. Biotechnol. 31, 46–53. 10.1038/nbt.2450 [PubMed: 23222703]

Trapnell C, Williams BA, Pertea G, Mortazavi A, Kwan G, Van Baren MJ, Salzberg SL, Wold BJ, Pachter L, 2010. Transcript assembly and quantification by RNA-Seq reveals unannotated transcripts and isoform switching during cell differentiation. Nat. Biotechnol. 28, 511–515. 10.1038/nbt.1621 [PubMed: 20436464]

Trompouki E, Bowman TV, Lawton LN, Fan ZP, Wu D-C, DiBiase A, Martin CS, Cech JN, Sessa AK, Leblanc JL, Li P, Durand EM, Mosimann C, Heffner GC, Daley GQ, Paulson RF, Young RA, Zon LI, 2011. Lineage Regulators Direct BMP and Wnt Pathways to Cell-Specific Programs during Differentiation and Regeneration. Cell 147, 577–589. [PubMed: 22036566]

van Wijk B, Moorman AFM, van den Hoff MJB, 2007. Role of bone morphogenetic proteins in cardiac differentiation. Cardiovasc. Res. 10.1016/j.cardiores.2006.11.022

Vokes SA, Ji H, McCuine S, Tenzen T, Giles S, Zhong S, Longabaugh WJR, Davidson EH, Wong WH, McMahon AP, 2007. Genomic characterization of Gli-activator targets in sonic hedgehog-mediated neural patterning. Development 134, 1977–1989. [PubMed: 17442700]

Vokes SA, Ji H, Wong WH, McMahon AP, 2008. A genome-scale analysis of the cis-regulatory circuitry underlying sonic hedgehog-mediated patterning of the mammalian limb. Genes Dev. 22, 2651–2663. 10.1101/gad.1693008 [PubMed: 18832070]

Wagner F, Barkley D, Yanai I, 2019. ENHANCE: Accurate denoising of single-cell RNA-Seq data. bioRxiv 655365. 10.1101/655365

Wang J, Cao J, Dickson AL, Poss KD, 2015. Epicardial regeneration is guided by cardiac outflow tract and Hedgehog signalling. Nature 522, 226–230. 10.1038/nature14325 [PubMed: 25938716]

Wang J, Greene SB, Bonilla-Claudio M, Tao Y, Zhang J, Bai Y, Huang Z, Black BL, Wang F, Martin JF, 2010. Bmp Signaling Regulates Myocardial Differentiation from Cardiac Progenitors Through a MicroRNA-Mediated Mechanism. Dev. Cell 19, 903–912. 10.1016/J.DEVCEL.2010.10.022 [PubMed: 21145505]

Wang Q, Zhao N, Kennard S, Lilly B, 2012. Notch2 and Notch3 Function Together to Regulate Vascular Smooth Muscle Development. PLOS ONE 7, e37365. 10.1371/JOURNAL.PONE.0037365 [PubMed: 22615991]

Watkins DN, Berman DM, Baylin SB, 2003. Hedgehog signaling: progenitor phenotype in small-cell lung cancer. Cell Cycle Georget. Tex 2, 196–198. 10.4161/cc.2.3.378

Watkins WS, Hernandez EJ, Wesolowski S, Bisgrove BW, Sunderland RT, Lin E, Lemmon G, Demarest BL, Miller TA, Bernstein D, Brueckner M, Chung WK, Gelb BD, Goldmuntz E, Newburger JW, Seidman CE, Shen Y, Yost HJ, Yandell M, Tristani-Firouzi M, 2019. De novo and recessive forms of congenital heart disease have distinct genetic and phenotypic landscapes. Nat. Commun. 10, 1–12. 10.1038/s41467-019-12582-y [PubMed: 30602773]

Weger M, Diotel N, Dorsemans A-C, Dickmeis T, Weger BD, 2017. Stem cells and the circadian clock. Dev. Biol. 431, 111–123. 10.1016/j.ydbio.2017.09.012 [PubMed: 28899666]

Wei Y, Ma D, Gao Y, Zhang C, Wang L, Liu F, 2014. Ncor2 is required for hematopoietic stem cell emergence by inhibiting Fos signaling in zebrafish. Blood 124, 1578–1585. 10.1182/BLOOD-2013-11-541391 [PubMed: 25006126]

Weintraub AS, Li CH, Zamudio AV, Sigova AA, Hannett NM, Day DS, Abraham BJ, Cohen MA, Nabet B, Buckley DL, Guo YE, Hnisz D, Jaenisch R, Bradner JE, Gray NS, Young RA, 2017. YY1 Is a Structural Regulator of Enhancer-Promoter Loops. Cell 171, 1573–1588.e28. 10.1016/J.CELL.2017.11.008 [PubMed: 29224777]

Welsh IC, Kwak H, Chen FL, Werner M, Shopland LS, Danko CG, Lis JT, Zhang M, Martin JF, Kurpios NA, 2015. Chromatin Architecture of the Pitx2 Locus Requires CTCF- and Pitx2-Dependent Asymmetry that Mirrors Embryonic Gut Laterality. Cell Rep. 13, 337–349. 10.1016/j.celrep.2015.08.075 [PubMed: 26411685]

Wicking C, Smyth I, Bale A, 1999. The hedgehog signalling pathway in tumorigenesis and development. Oncogene 18, 7844–7851. 10.1038/sj.onc.1203282 [PubMed: 10630637]

Wilson GN, 1988. Heterochrony and human malformation. Am. J. Med. Genet. 29, 311–321. 10.1002/ajmg.1320290210 [PubMed: 3281459]

Wolf FA, Angerer P, Theis FJ, 2018. SCANPY: Large-scale single-cell gene expression data analysis. Genome Biol. 19, 15. 10.1186/s13059-017-1382-0 [PubMed: 29409532]

Xiang M, Gan L, Zhou L, Klein WH, Nathans J, 1996. Targeted deletion of the mouse POU domain gene Brn-3a causes a selective loss of neurons in the brainstem and trigeminal ganglion, uncoordinated limb movement, and impaired suckling. Proc. Natl. Acad. Sci. U. S. A. 93, 11950–11955. 10.1073/PNAS.93.21.11950 [PubMed: 8876243]

Xie L, Hoffmann AD, Burnicka-Turek O, Friedland-Little JM, Zhang K, Moskowitz IP, 2012. Tbx5-Hedgehog Molecular Networks Are Essential in the Second Heart Field for Atrial Septation. Dev. Cell 23, 280–291. [PubMed: 22898775]

Yang J, Bücker S, Jungblut B, Böttger T, Cinnamon Y, Tchorz J, Müller M, Bettler B, Harvey R, Sun QY, Schneider A, Braun T, 2012. Inhibition of Notch2 by Numb/Numblike controls myocardial compaction in the heart. Cardiovasc. Res. 96, 276–285. 10.1093/CVR/CVS250 [PubMed: 22865640]

Ying QL, Stavridis M, Griffiths D, Li M, Smith A, 2003. Conversion of embryonic stem cells into neuroectodermal precursors in adherent monoculture. Nat. Biotechnol. 2003 212 21, 183–186. 10.1038/nbt780

Zhan X, Shi X, Zhang Z, Chen Y, Wu JI, 2011. Dual role of Brg chromatin remodeling factor in Sonic hedgehog signaling during neural development 108, 12758–12763.

Zhang Y, Liu T, Meyer CA, Eeckhoute J, Johnson DS, Bernstein BE, Nussbaum C, Myers RM, Brown M, Li W, Shirley XS, 2008. Model-based analysis of ChIP-Seq (MACS). Genome Biol. 9, R137. 10.1186/gb-2008-9-9-r137 [PubMed: 18798982]

Zhang Y, Xiang Y, Yin Q, Du Z, Peng X, Wang Q, Fidalgo M, Xia W, Li Y, Zhao ZA, Zhang W, Ma J, Xu F, Wang J, Li L, Xie W, 2017. Dynamic epigenomic landscapes during early lineage specification in mouse embryos. Nat. Genet. 2017 501 50, 96–105. 10.1038/s41588-017-0003-x

Zhao H, Feng J, Seidel K, Shi S, Klein O, Sharpe P, Chai Y, 2014. Secretion of shh by a neurovascular bundle niche supports mesenchymal stem cell homeostasis in the adult mouse incisor. Cell Stem Cell 14, 160–173. 10.1016/j.stem.2013.12.013 [PubMed: 24506883]

Zhao Y, Kwan KM, Mailloux CM, Lee WK, Grinberg A, Wurst W, Behringer RR, Westphal H, 2007. LIM-homeodomain proteins Lhx1 and Lhx5, and their cofactor Ldb1, control Purkinje cell differentiation in the developing cerebellum. Proc. Natl. Acad. Sci. U. S. A. 104, 13182–13186. 10.1073/PNAS.0705464104 [PubMed: 17664423]

Zhou Y, Zhou B, Pache L, Chang M, Khodabakhshi AH, Tanaseichuk O, Benner C, Chanda SK, 2019. Metascape provides a biologist-oriented resource for the analysis of systems-level datasets. Nat. Commun. 10, 1–10. 10.1038/s41467-019-09234-6 [PubMed: 30602773]

Zhu F, Farnung L, Kaasinen E, Sahu B, Yin Y, Wei B, Dodonova SO, Nitta KR, Morgunova E, Taipale M, Cramer P, Taipale J, 2018. The interaction landscape between transcription factors and the nucleosome. Nature 562, 76–81. 10.1038/s41586-018-0549-5 [PubMed: 30250250]

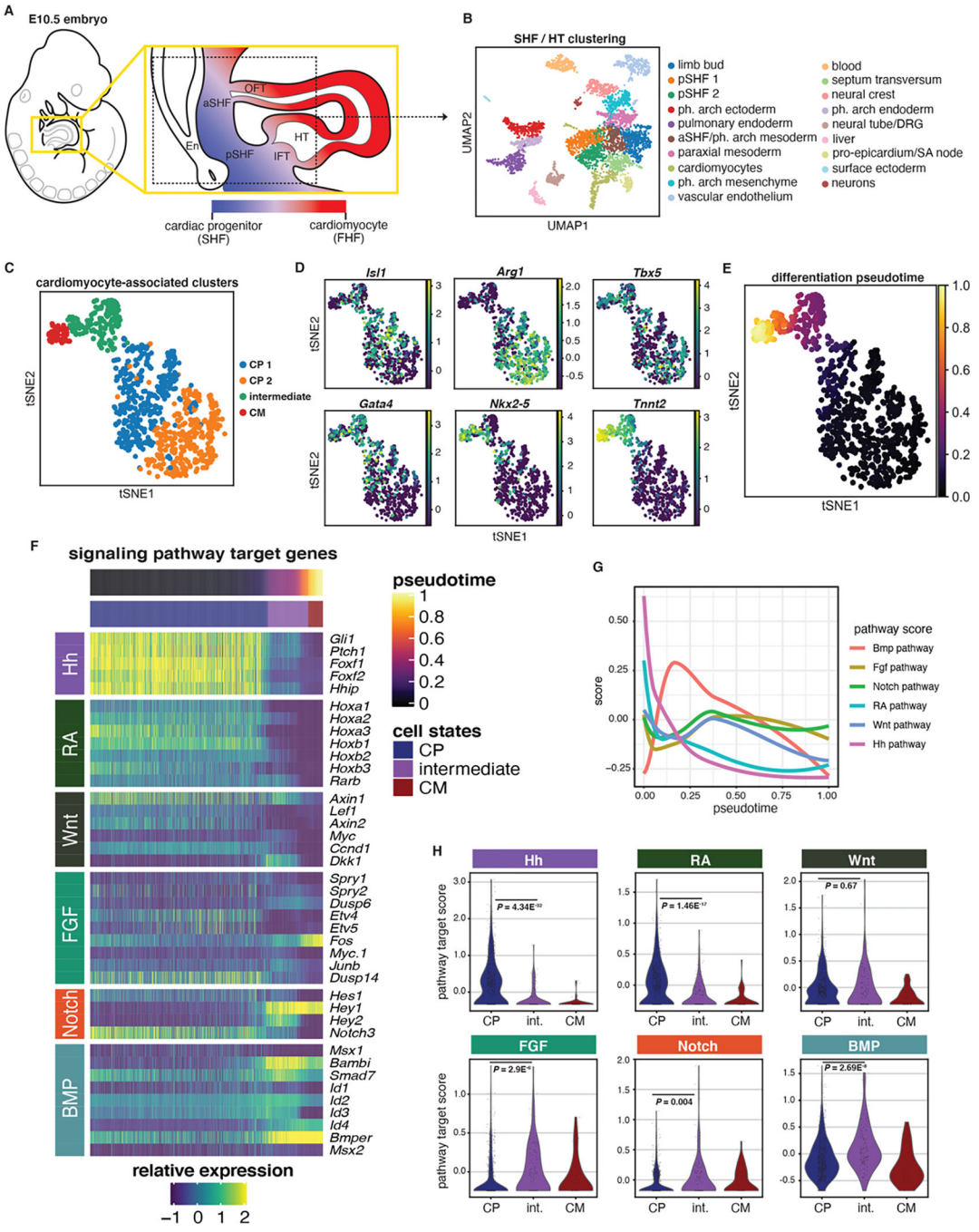

Figure 1. Hedgehog signaling is specific to cardiac progenitors during cardiac differentiation *in vivo*.

(A) Diagram of Second Heart Field (SHF) and Heart Tube (HT) regions of an E10.5 mouse embryo. Dotted lines indicate the boundaries of microdissection for Drop-seq experiment (*N* = 2). **(B)** UMAP plot displaying 19 distinct cell type clusters identified from microdissected SHF and HT tissue. **(C)** tSNE plot showing 4 cardiac-associated clusters of pSHF and HT cells. **(D)** tSNE plots indicating the expression levels of cardiac transcription factors and CP/CM marker genes within the 4 CM-associated clusters. **(E)** Cardiac differentiation

pseudotime (dpt) score indicated by cell color within tSNE plot of 4 cardiac-associated clusters. **(F)** Heatmap of individual cells from cardiac-associated Drop-seq clusters showing the denoised expression levels of target genes of 6 signaling pathways along the pseudotime differentiation trajectory. **(G)** Line plot indicating the aggregated relative expression levels of pathway target genes along the pseudotime differentiation trajectory. **(H)** Violin plots showing the metagene scores for signaling pathway target genes at the CP, intermediate and CM stages of cardiac differentiation for 6 signaling pathways. Int., intermediate; aSHF, anterior second heart field; pSHF, posterior second heart field; OFT, outflow tract; IFT, inflow tract; En, pulmonary endoderm.

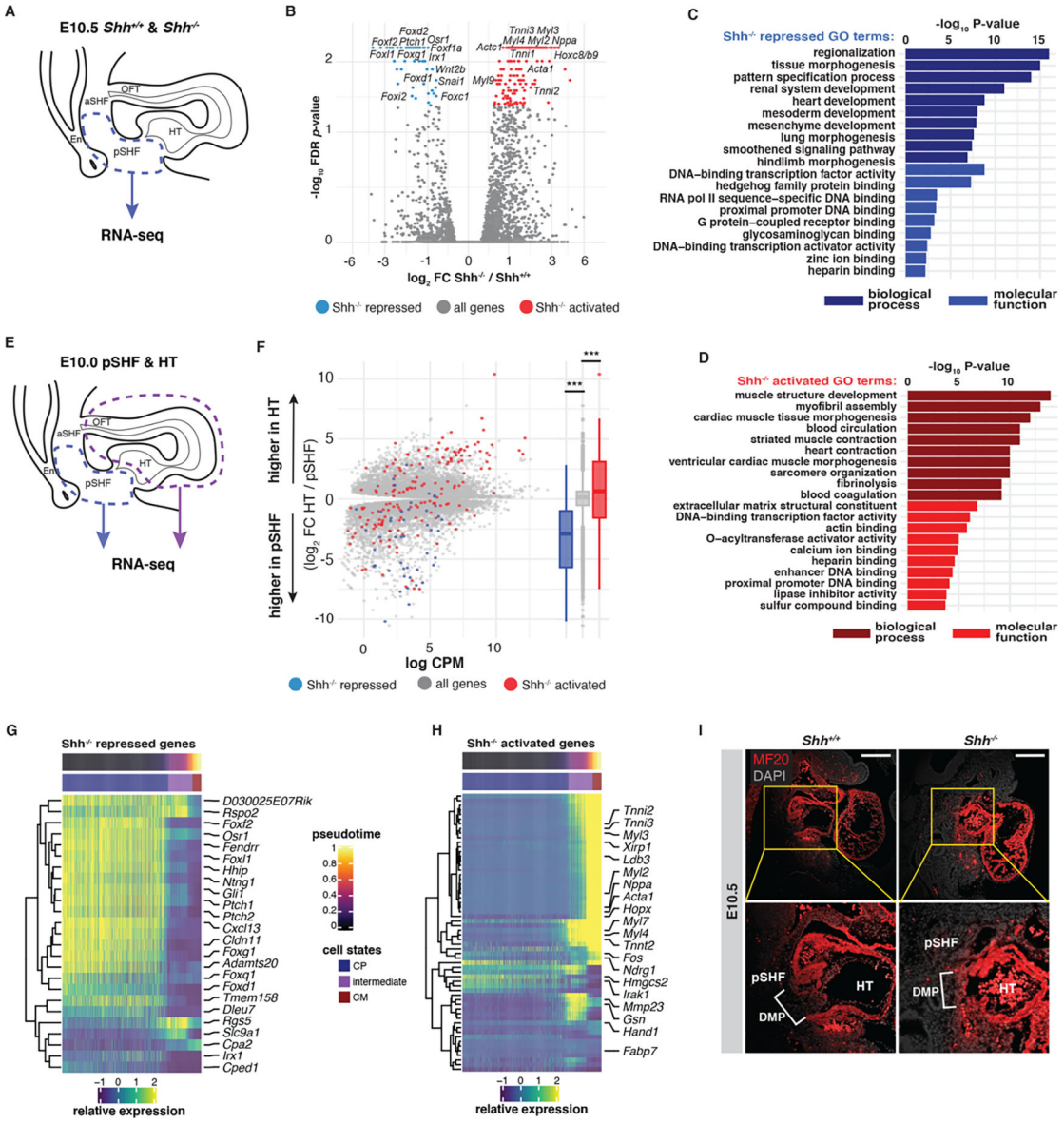

Figure 2. Hedgehog signaling prevents premature activation of the cardiac differentiation program in the second heart field.

(A) Diagram of the SHF and HT regions of an E10.5 mouse embryo. Dotted lines indicate the boundaries of microdissection for a SHF-specific RNA-seq from $Shh^{+/+}$ and $Shh^{-/-}$ embryos ($N = 4–5$). **(B)** Volcano plot displaying activated and repressed genes in the $Shh^{-/-}$ relative to $Shh^{+/+}$ pSHF. Red and blue dots signify significantly upregulated and downregulated genes, respectively. **(C)** Gene ontology (GO) analysis of $Shh^{-/-}$ repressed genes. **(D)** Gene ontology (GO) analysis of $Shh^{-/-}$ activated genes. **(E)** Diagram of the SHF and HT regions of an E10.0 mouse embryo with dotted lines that indicate the boundaries of microdissection for RNA-seq comparing the pSHF and HT ($N = 6$). **(F)** MA plot and box plots illustrating the distribution of $Shh^{-/-}$ dysregulated genes superimposed on the distribution of differentially expressed genes between the wild type pSHF and HT. **(G)** Heatmap showing the wild type expression levels of $Shh^{-/-}$ repressed genes

along the pseudotime differentiation trajectory from cardiac-associated Drop-seq clusters. **(H)** Heatmap showing the wild type expression levels of $Shh^{-/-}$ activated genes along the pseudotime differentiation trajectory from cardiac-associated Drop-seq clusters. **(I)** Immunofluorescent staining for sarcomeric myosin (MF20) in the E10.5 pSHF of $Shh^{+/+}$ and $Shh^{-/-}$ embryos. MF20 staining is shown in red and DAPI counterstain is shown in grey. White bracket demarcates the forming DMP ($N = 3–4$). Scale bars = 200μm. DMP, dorsal mesenchymal protrusion. *** $P \leqq 0.005$.

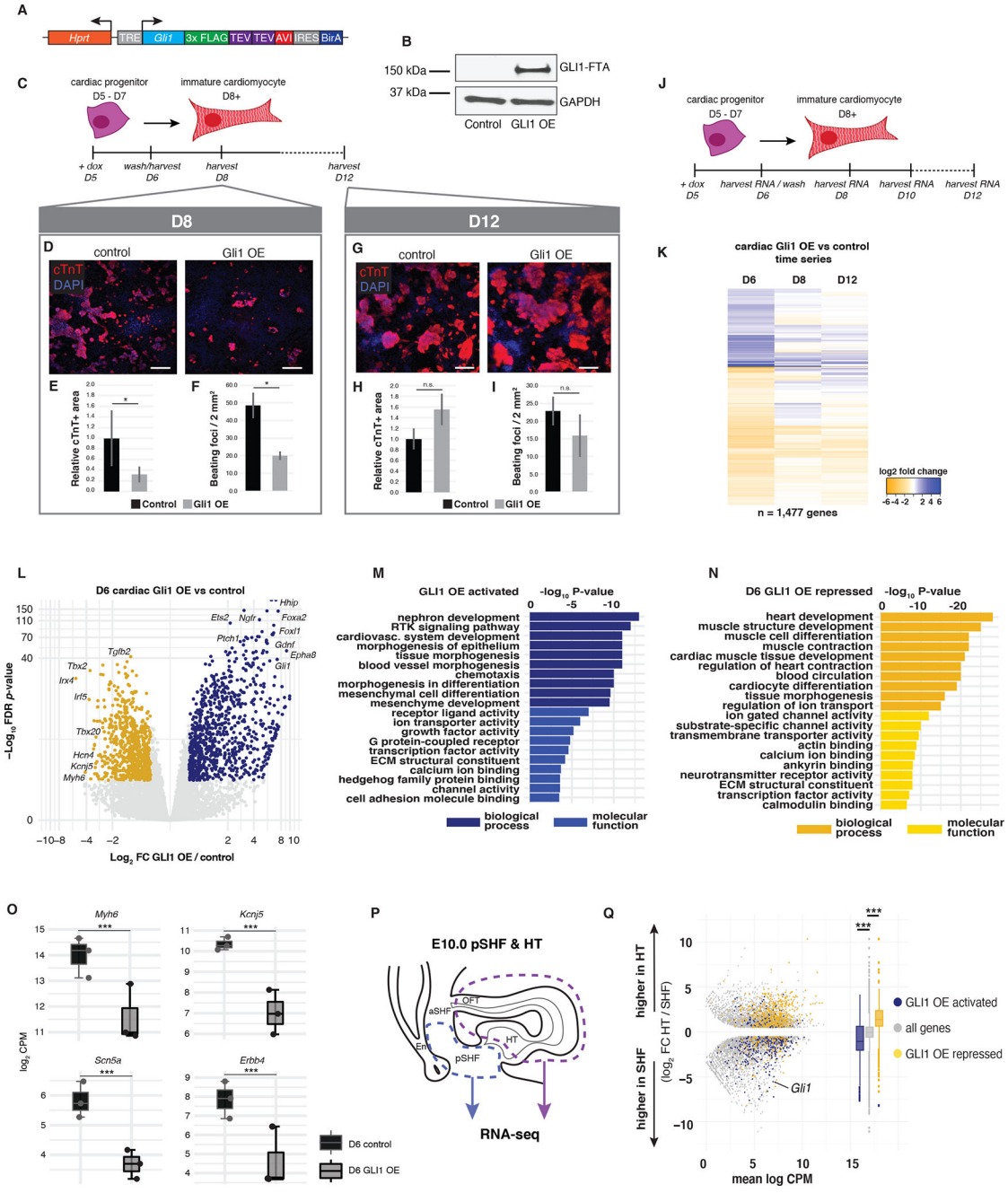

Figure 3. The Hh signaling transcription factor GLI1 is sufficient to delay cardiomyocyte differentiation *in vitro*.

(A) Diagram of a doxycycline-inducible GLI1-FTA transgenic cassette inserted into the *Hprt* locus in mESCs. **(B)** Western blot showing induction of GLI1 protein, a marker of active Hh signaling, after doxycycline treatment for 24 hours in CPs. **(C)** Schematic representation of the experimental design employed for transient GLI1 overexpression (GLI1 OE) in mESC-derived CM differentiations. **(D)** Immunofluorescent staining for cardiac troponin (cTnT) in control and GLI1 OE cells harvested at D8. cTnT staining is shown in red and DAPI staining is shown in blue. Scale bar = 100μm. **(E)** Quantification of the area of cTnT-positivity in

control and GLI1 OE cells at D8 ($N = 10$). **(F)** Quantification of the number of beating foci in videos of control and GLI1 OE cells at D8 ($N = 10$). **(G)** Immunofluorescent staining for cardiac troponin in control and GLI1 OE cells harvested at D12. cTnT staining is shown in red and DAPI staining is shown in blue. Scale bar = 100μm. **(H)** Quantification of the area of cTnT-positivity in control and GLI1 OE cells at D12 ($N = 10$). **(I)** Quantification of the number of beating foci in videos of control and GLI1 OE cells at D12 ($N = 10$). **(J)** Schematic representation of transient GLI1 overexpression (GLI1 OE) experimental design in mESC-derived CM differentiation for RNA-seq time series analysis. **(K)** Time-series heatmap of differentially expressed genes in GLI1 OE CPs relative to control differentiations at D6, D8 and D12 ($N = 2–4$). **(L)** Volcano plot displaying activated and repressed genes in GLI1 OE CPs relative to control CPs embryos at D6. Blue and yellow dots signify significantly activated and repressed genes, respectively ($N = 4$). **(M)** Gene ontology (GO) analysis of GLI1 OE activated genes at D6. **(N)** Gene ontology (GO) analysis of GLI1 OE repressed genes at D6. **(O)** Boxplots showing repression of cardiac differentiation markers in GLI1 OE mESC-CPs at D6. **(P)** Diagram of the SHF and HT regions of an E10.0 mouse embryo with dotted lines that indicate the boundaries of microdissection for RNA-seq experiment comparing the pSHF and HT of E10.0 wild type embryos ($N = 6$). **(Q)** MA plot with box plots illustrating the distribution of GLI1 OE dysregulated genes superimposed on the distribution of differential expression between the wild type E10.0 pSHF and HT. n.s., not significant. * $P \leqq 0.05$, *** $P \leqq 0.005$.

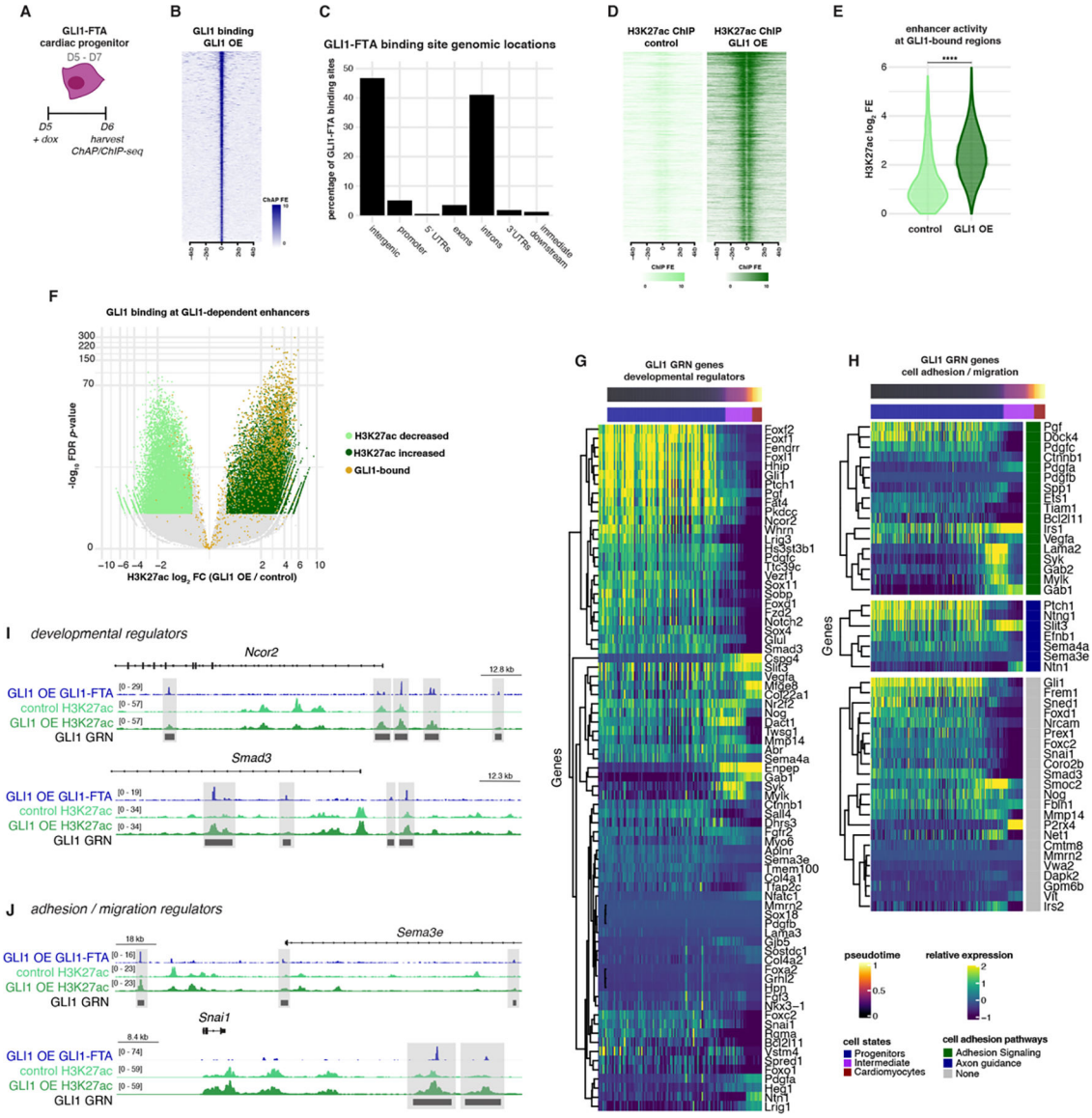

Figure 4. GLI1 directly activates a GRN comprised of progenitor genes controlled by distal enhancers.

(A) Schematic representation of experimental design for ChAP/ChIP-seq in GLI1 overexpression (GLI1 OE) mESC-derived cardiac differentiations ($N = 2$). **(B)** Heatmap showing GLI1-FTA ChAP-seq signal Z-scores in mESC-CPs at D6 at all GLI1-bound regions. **(C)** Bar plot revealing the percentage of D6 GLI1-bound regions annotated to genomic features. **(D)** Heatmap showing the H3K27ac ChIP-seq signal Z-scores in mESC-CPs at D6 at all GLI1-bound regions. **(E)** Violin plot depicting the fold enrichment over input of H3K27ac ChIP-seq signal at GLI1-bound regions in D6 control and GLI1 OE conditions. **(F)** Volcano plot displaying activated and deactivated enhancers in GLI1 OE CPs relative to control CPs embryos at D6. Gold dots label all GLI1-bound regions. **(G)** Heatmap of individual cells from cardiac-associated Drop-seq clusters showing the denoised expression levels of GLI1 GRN genes associated with developmental regulation along the pseudotime differentiation trajectory. **(H)** Heatmap of individual cells from cardiac-

associated Drop-seq clusters showing the denoised expression levels of GLI1 GRN genes associated with cell adhesion or migration along the pseudotime differentiation trajectory. **(I)** Genome browser view of the GLI1 GRN developmental regulators *Ncor2* and *Smad3*, with H3K27ac signal enrichment in D6 control and GLI1 OE. GLI1 GRN enhancers are highlighted in grey boxes. **(J)** Genome browser view of the GLI1 GRN adhesion/migration regulators *Sema3e* and *Snai1*, with H3K27ac signal enrichment in D6 control and GLI1 OE. GLI1 GRN enhancers are highlighted in grey boxes. GRN, gene regulatory network. **** $P \leqq 0.001$.

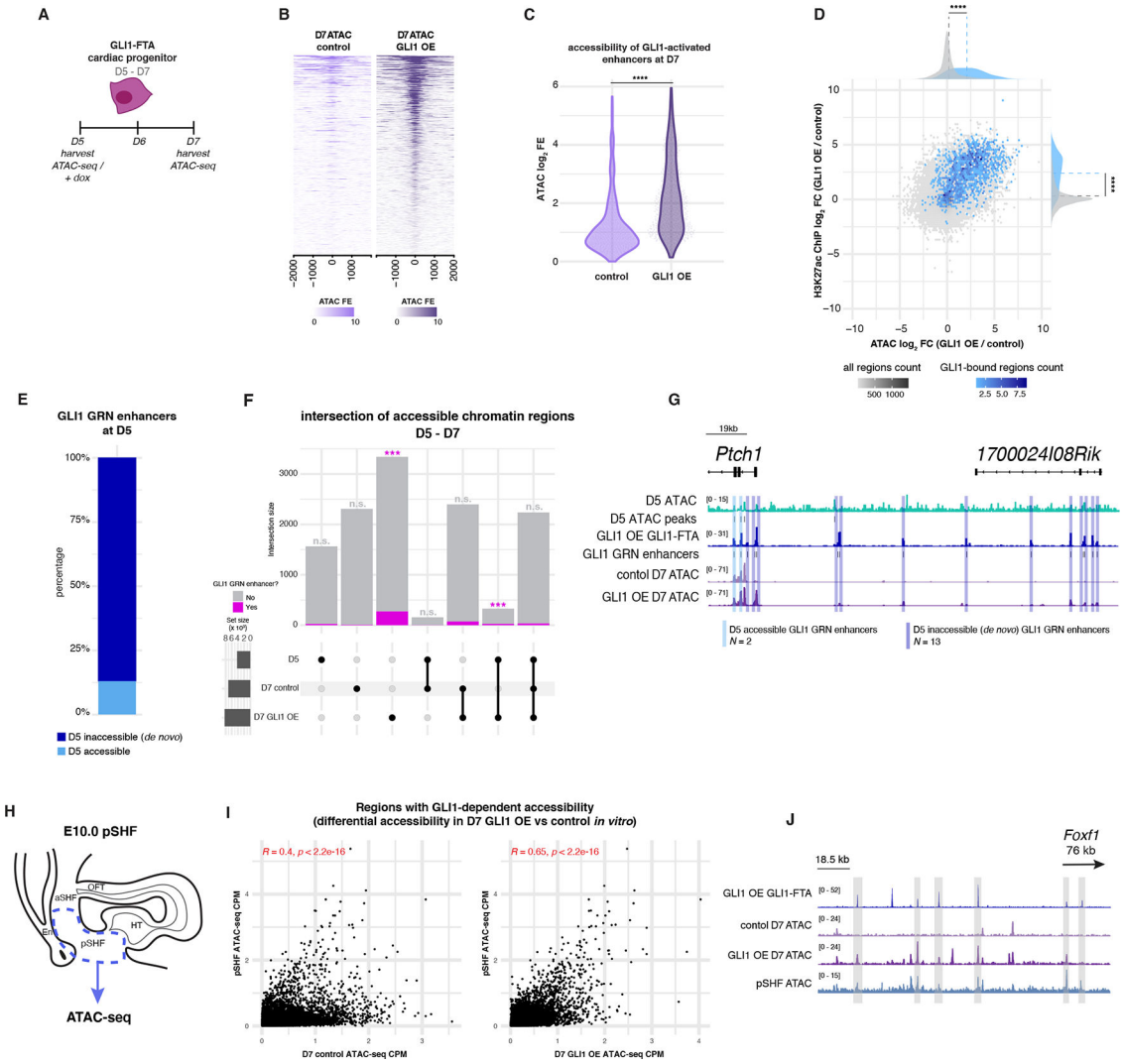

Figure 5. The GLI1 GRN is pSHF-like and is activated *de novo* in mESC-CPs.

(A) Schematic representation of experimental design for ATAC-seq in GLI1 overexpression (GLI1 OE) mESC-derived cardiac differentiations ($N = 2$). **(B)** Heatmap showing the ATAC-seq signal Z-scores in mESC-CPs at D7 at GLI1 GRN enhancers. **(C)** Violin plot depicting the fold enrichment over background of ATAC-seq signal at GLI1 GRN enhancers in D7 control and GLI1 OE conditions. **(D)** Density plot showing the GLI1-mediated $\log_2$FC in ATAC-seq and H3K27ac ChIP-seq enrichment for all putative regulatory regions in D6 and D7 mESC-CPs. Blue hexes label all GLI1-bound regions. **(E)** Bar plot depicting the proportion of GLI1 GRN enhancers demonstrating accessibility at D5 prior to GLI1 OE. **(F)** Upset plot showing the intersection of accessible regions in D5, D7 control and D7 GLI1 OE conditions. Pink bars represent the regions in each intersection bin that are GLI1 GRN enhancers. **(G)** GLI1-FTA ChAP-seq and ATAC-seq signal fold enrichment over input near the GLI1 target gene, *Ptch1*. GLI1 GRN enhancers with D5 accessibility ($N = 2$) are highlighted in blue boxes, and *de novo* accessible GLI1 GRN enhancers ($N = 13$) are highlighted in purple boxes. **(H)** Diagram of the SHF and HT of an E10.0 mouse embryo with dotted lines that indicate the boundaries of microdissection for a pSHF-specific

ATAC-seq ($N = 3$). **(I)** Scatterplots of normalized ATAC-seq counts comparing accessibility between D7 control and D7 GLI1 OE *in vitro,* and the *in vivo* pSHF. **(J)** Genome browser view of a locus 76kb upstream of *Foxf1*, a GLI1 GRN gene, with ATAC-seq data from D7 control and GLI1 OE *in vitro* and the *in vivo* pSHF. GLI1 GRN enhancers that demonstrate *de novo* accessibility due to GLI1 in mESC-CPs are highlighted in grey boxes. *** $P \leqq 0.001$.

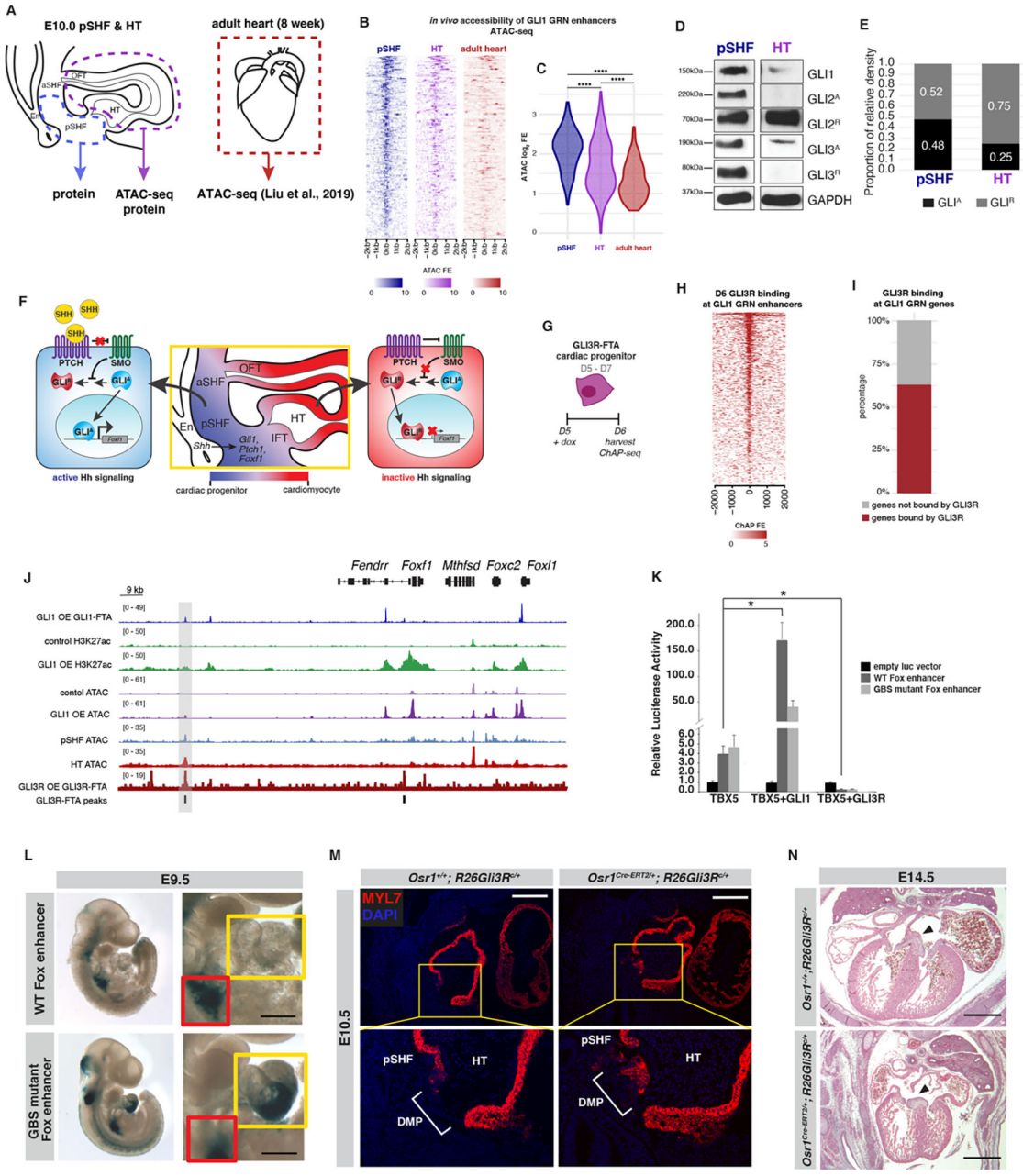

Figure 6. A GLI TF transition restricts the heterochronic GRN to the SHF and prevents Congenital Heart Disease.

(A) Diagram of the SHF and HT regions of an E10.0 mouse embryo and an adult mouse heart with dotted lines that indicate the boundaries of microdissection for ATAC-seq or protein isolation ($N = 3$). **(B)** Heatmap showing ATAC-seq signal Z-scores in the pSHF, HT and adult heart at GLI1 GRN enhancers. **(C)** Violin plot comparing mean ATAC-seq fold enrichment in the pSHF, HT and adult heart at GLI1 GRN enhancers. **(D)** Western blot demonstrating the expression level of GLI^A and GLI^R proteins in the E10.0 wild type pSHF and HT. **(E)** Bar plot showing the relative proportion of GLI^A and GLI^R proteins in the E10.0 wild type pSHF and HT, from (D). **(F)** Schematic of a model describing how Hh

GLI^{A} and GLI^{R} TFs could regulate GLI1 GRN genes in a spatiotemporal manner in the mouse embryo to control SHF CM differentiation timing **(G)** Schematic representation of experimental design for ChAP-seq in GLI3^{R}-FTA overexpression (GLI3 OE) mESC-derived cardiac differentiations ($N = 2$). **(H)** Heatmap showing GLI3^{R}-FTA ChAP-seq signal Z-scores in mESC-CPs at D6 at all *in vivo*-accessible GLI1 GRN enhancers. **(I)** Bar plot depicting the proportion of GLI1 GRN genes with GLI3^{R}-FTA binding within 200kb of the TSS. **(J)** Genome browser view of the *Foxf1* locus showing the *Foxf1* TSS and a GLI1 GRN enhancer upstream of the TSS (grey box, Fox enhancer). **(K)** Bar plots depicting luciferase reporter activity resulting from co-transfection of TBX5 with either GLI1 or GLI3^{R} ($N = 3$). **(L)** Transient transgenic analysis of *lacZ* reporter expression in the E10.0 pSHF (red box) and HT (gold box) driven by wild type and GLI binding site mutant versions of the Fox enhancer ($N = 5–8$). **(M)** Immunofluorescent staining for MYL7 in the E10.5 pSHF from control and GLI3^{R} OE embryos (blue = DAPI, red = MYL7). White bracket demarcates the forming DMP ($N = 3$). Scale bars = 200μm. **(N)** Histological sections of E14.5 hearts from control and GLI3^{R} OE embryos. Black arrowheads highlight incidence of AVSD ($N = 5$). Scale bars = 200μm. GBS, GLI binding site. * $P \leqq 0.05$, **** $P \leqq 0.001$.

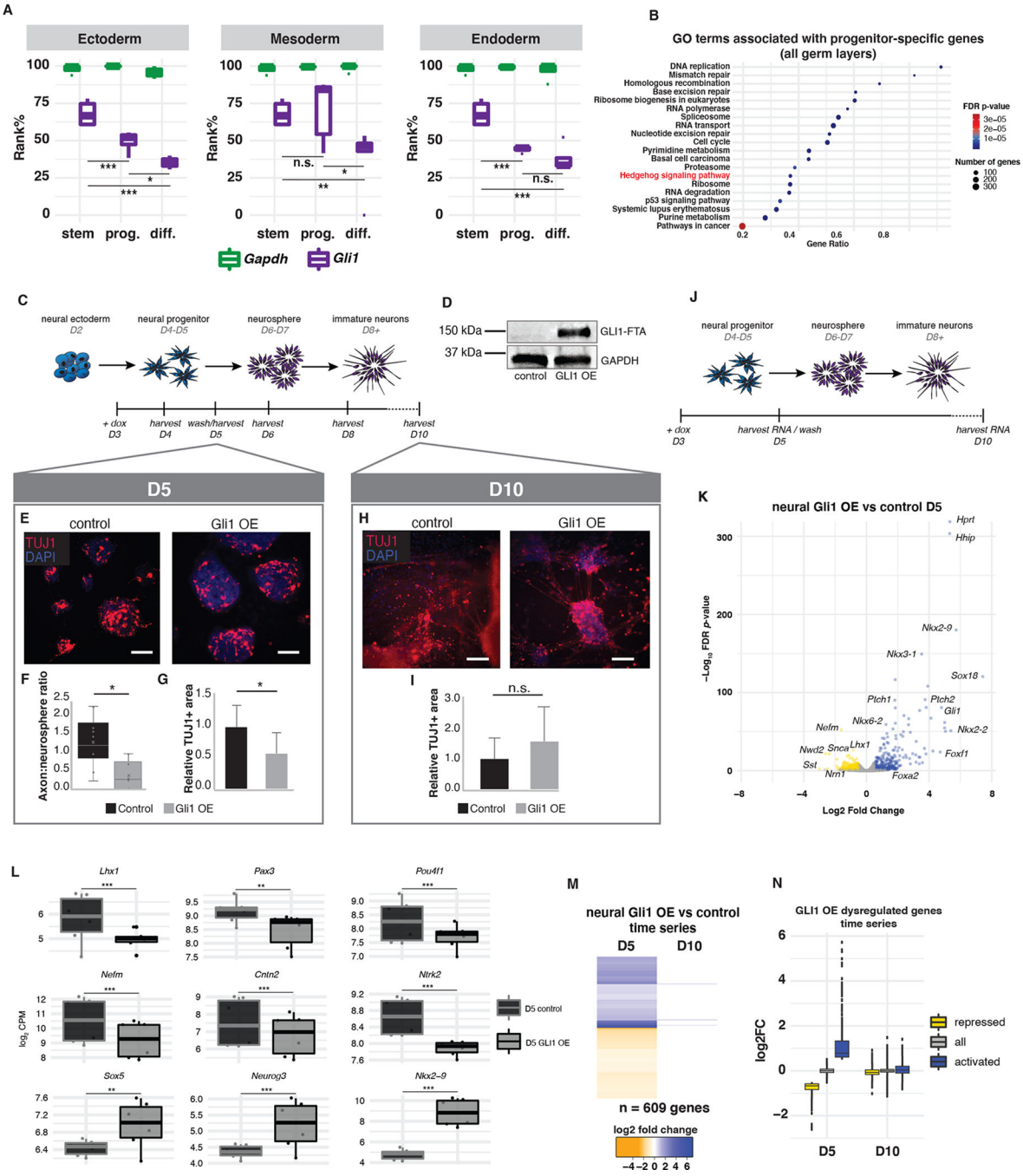

Figure 7. GLI1 expression in neural progenitors transiently delays neuronal differentiation.

(A) Gene expression rankings for *Gli1* and *Gapdh* from transcriptional profiling of mouse germ layer-specific differentiation series (N = 2–6). **(B)** Dot plot of GO term analysis of genes expressed more highly in progenitor cells than in differentiated cells across all germ layers in mice. **(C)** Schematic representation of the transient GLI1 OE experimental design in mESC-derived differentiating neurons. **(D)** Western blot showing induction of GLI1 protein expression in neural progenitors after doxycycline treatment for 48 hours. **(E)** Immunofluorescent staining for pan-neuronal marker TUJ1 in control and GLI1 OE

cells harvested at D5. TUJ1 staining is shown in red and DAPI counterstain is shown in blue. Scale bar = 100μm. **(F)** Quantification of the ratio of axons to neurospheres in control and GLI1 OE cells at D5 ($N = 10$). **(G)** Quantification of the area of TUJ1-positivity in control and GLI1 OE cells at D5 ($N = 10$). **(H)** Immunofluorescent staining for TUJ1 in control and GLI1 OE cells harvested at D10. TUJ1 staining is shown in red and DAPI counterstain is shown in blue. Scale bar = 100μm. **(I)** Quantification of the area of TUJ1-positivity in control and GLI1 OE cells at D10 ($N = 10$). **(J)** Schematic representation of the transient GLI1 overexpression (GLI1 OE) experimental design in mESC-derived differentiating neurons for RNA-seq time series ($N = 3$). **(K)** Volcano plot displaying activated and repressed genes in GLI1 OE neural progenitors relative to control neural progenitors at D5. Blue and yellow dots signify significantly dysregulated genes. **(L)** Boxplots showing repression of neurogenic TFs (top) and neural differentiation products (middle) and activation of neural progenitor TFs (bottom) in GLI1 OE mESC-NPs at D5. **(M)** Time-series heatmap of the $\log_2$ FC values of genes differentially expressed in GLI1 OE neural cells relative to control at D5 and at D10. **(N)** Boxplots showing a time series of the mean $\log_2$ fold change of genes activated and repressed by GLI1 OE in neural cells at Day 5 and Day 10, relative to all genes. * $P \leqq 0.05$, ** $P \leqq 0.01$, *** $P \leqq 0.005$.

KEY RESOURCES TABLE

REAGENT or RESOURCE	SOURCE	IDENTIFIER
Antibodies		
Rabbit polyclonal anti-GLI1	Cell Signaling Technology	Cat# 2534S; RRID: AB_2294745
Goat polyclonal anti-GLI3	R&D Systems	Cat# AF3690; RRID: AB_2232499
Mouse monoclonal anti-GAPDH	Abcam	Cat# ab8245; RRID: AB_2107448
Mouse monoclonal anti-FLAG	MilliporeSigma	Cat# F3165; RRID: AB_259529; Clone M2
Mouse monoclonal anti-Troponin T	Fisher Scientific	Cat# MS295P1; RRID: AB_61808; Clone 13-11
Mouse monoclonal anti-Troponin T BV421	BD Biosciences	Cat# 562438; RRID: AB_2739306; Clone 13-11
Mouse monoclonal anti-IgG1, k isotype BV421	BD Biosciences	Cat# 562438; RRID: AB_11207319; Clone X40
Rat monoclonal anti-Ki67	Thermo Fisher	Cat# 14-5698-80; RRID: AB_10854564; Clone SolA15
Rabbit polyclonal anti-GLI2	Cell Signaling Technology	Cat# 2585S; RRID: AB_2294767
Mouse monoclonal anti-myosin heavy chain	Developmental Studies Hybridoma Bank	Cat# MF20; RRID: AB_1293549; Clone MF20
Rabbit polyclonal anti-MYL7	Thermo Fisher	Cat# 17283-1-AP; RRID: AB_2250998
Mouse monoclonal anti-beta-III Tubulin	R&D Systems	Cat# MAB1195; RRID: AB_357520; Clone TuJ-1
Rat monoclonal anti-CD140a (PDGFRa) PE	Thermo Fisher	Cat# 12-1401-81
Rat monoclonal anti-CD309 (FLK-1) PE-Cy7	BioLegend	Cat# 136414
Mouse monoclonal anti-H3K27ac	FUJIFILM Wako	Cat# 306-34849; RRID: AB_10552905; Clone MABI0309
Bacterial and virus strains		
DH5α subcloning efficiency competent cells	Thermo Fisher	Cat# 18265017
Chemicals, peptides, and recombinant proteins		
Neurobasal medium	Thermo Fisher	Cat# 21103049
DMEM/F12 medium	Thermo Fisher	Cat# 10565018
Iscove's modified Dubelcco's medium (IMDM)	Thermo Fisher	Cat# 31980030
Ham's F12 medium	Thermo Fisher	Cat# 31765035
Stempro-34 SF medium	Thermo Fisher	Cat# 10639011
N2 supplement (100x)	Thermo Fisher	Cat# 17502048
B27 supplement (50x)	Thermo Fisher	Cat# 17504044
Penicillin-Streptomycin	Thermo Fisher	Cat# 15140122
L-Glutamine	Thermo Fisher	Cat# 25030081
1-Thioglycerol	MilliporeSigma	Cat# M6145
Bovine serum albumin solution (30%)	MilliporeSigma	Cat# A9576
Leukemia Inhibitory Factor (LIF)	MilliporeSigma	Cat# ESG1106
PD0325901 (Mirdametinib)	Selleck Chemicals	Cat# S1036
CHIR-99021 (Laduviglusib)	Selleck Chemicals	Cat# S1263

REAGENT or RESOURCE	SOURCE	IDENTIFIER
L-ascorbic Acid	MilliporeSigma	Cat# A4544
Transferrin, human	MilliporeSigma	Cat# T8158
Recombinant human basic FGF	R&D Systems	Cat# 233-FB-010
Recombinant human BMP4	R&D Systems	Cat# 314-BP-010
Recombinant human/mouse/rat Activin A	R&D Systems	Cat# 338-AC-010
Recombinant mouse VEGF	R&D Systems	Cat# 493-MV-005
GlutaMAX supplement	Thermo Fisher	Cat# 35050061
Normocin	InvivoGen	Cat# ant-nr-1
Propidium Iodide	Thermo Fisher	Cat# P3566
TrypLE Express	Thermo Fisher	Cat# 12605010
Fetal bovine serum, heat inactivated	Thermo Fisher	Cat# 10438026
EmbryoMax 0.1% gelatin solution	MilliporeSigma	Cat# ES-006-B
TRIzol reagent	Thermo Fisher	Cat# 15596026
Cell Lysis Buffer (10x)	Cell Signaling Technologies	Cat# 9803S
ECL Western blotting substrate	Thermo Fisher	Cat# 32106
Doxycycline hyclate	MilliporeSigma	Cat# D9891
Tamoxifen	MilliporeSigma	Cat# T5648
Critical commercial assays		
BCA Protein Assay kit	Thermo Fisher	Cat# 23225
RNeasy Mini Kit	Qiagen	Cat# 74104
TruSeq RNA library prep kit v2	Illumina	Cat# RS-122-2001
iTaq universal SYBR green one-step kit	Bio-rad	Cat# 1725151
NucleoSpin RNA mini kit	Macherey-Nagel	Cat# 740955.250
Fixation/permeabilization kit	BD Biosciences	Cat# 554714
NEBNext Ultra II DNA Library prep kit for Illumina	New England Biolabs	Cat# E7370S
Nextera XT DNA Library prep kit	Illumina	Cat# FC-131-1096
Dual-Luciferase reporter assay system	Promega	Cat# E1960
Deposited data		
Drop-seq scRNA-seq data from E10.0 CD1 mouse SHF	This paper	GEO: GSE196095
Bulk RNA-seq data from E10.5 *Shh*$^{+/+}$ & *Shh*$^{-/-}$ mouse pSHF	This paper	GEO: GSE196095
Bulk RNA-seq data from E10.0 CD1 mouse pSHF & HT	This paper	GEO: GSE196095
Bulk ATAC-seq data from E10.0 CD1 mouse pSHF & HT	This paper	GEO: GSE196095
Bulk RNA-seq data from D5-D12 mESC-CM differentiation time course	This paper	GEO: GSE196095
Bulk RNA-seq data from D6-D12 GLI1 OE and control cardiac differentiations	This paper	GEO: GSE196095
Bulk ATAC-seq data from D5-7 GLI1 OE and control mESC-CPs	This paper	GEO: GSE196095
GLI1-FTA and H3K27ac ChIP-seq data from D6 GLI1 OE and control mESC-CPs	This paper	GEO: GSE196095
GLI3R-FTA ChIP-seq data from D6 GLI1 OE and control mESC-CPs	This paper	GEO: GSE196095

REAGENT or RESOURCE	SOURCE	IDENTIFIER
Bulk RNA-seq data from D5-D10 GLI1 OE and control neural differentiations	This paper	GEO: GSE196095
Experimental models: Cell lines		
Mouse: GLI1-FTA transgenic A2Lox.cre mESC line	This paper	N/A
Mouse: GLI3R-FTA transgenic A2Lox.cre mESC line	This paper	N/A
Human: HEK293T cells	ATCC	Cat# CRL-3216; RRID: CVCL_0063
Experimental models: Organisms/strains		
Mouse: *Shh*$^{-/-}$: *Shh*^{tm1Amc}/J	The Jackson Laboratory	Strain# 003318; RRID:IMSR_JAX:003318
Mouse: *Osr1*$^{eGFPCre-ERT2}$: *Osr1*$^{tm1(EGFP/cre/ERT2)Amc}$/J	The Jackson Laboratory	Strain# 009061; RRID:IMSR_JAX:009061
Mouse: *ROSA26*$^{Gli3R-Flag}$: *Gt(ROSA)26Sor*$^{tm3(Gli3)Amc}$/J	The Jackson Laboratory	Strain# 013124; RRID:IMSR_JAX:013124
Mouse: CD-1 IGS	Charles River	Strain# Crl: CD1 (ICR)
Oligonucleotides		
qPCR primer: *Mus musculus Gli1* F: 5'- TGTGTGAGCAAGAAGGTTGC-3' R: 5'-ATGGCTTCTCATTGGAGTGG-3'	This paper	N/A
qPCR primer: *Mus musculus Gli2* F: 5'- GGTCAAGACTGAGGCTGAGG-3' R: 5'-TCATCCCTGTCCAGGTCTTC-3'	This paper	N/A
qPCR primer: *Mus musculus Gli3* F: 5'- GCAACCTCACTCTGCAACAA-3' R: 5'-CCTTGTGCCTCCATTTTGAT-3'	This paper	N/A
qPCR primer: *Mus musculus Ptch1* F: 5'- AATTCTCGACTCACTCGTCCA-3' R: 5'-CTCCTCATATTTGGGGCCTT-3'	This paper	N/A
qPCR primer: *Mus musculus Foxf1* F: 5'- AGCAGCCATACCTTCACCAA-3' R: 5'-CTGGGCGACTGTGAGTGATA-3'	This paper	N/A
qPCR primer: *Mus musculus Foxf2* F: 5'- GCGCTTCACCTTACCTCAAG-3' R: 5'-TGCAAGTAGCTCTGCTCCAA-3'	This paper	N/A
qPCR primer: *Mus musculus Fendrr* F: 5'- CTGCCCGTGTGGTTATAATG-3' R: 5'-TGACTCTCAAGTGGGTGCTG-3'	This paper	N/A
qPCR primer: *Mus musculus Isl1* F: 5'- TCATCCGAGTGTGGTTTCAA-3' R: 5'-TTCCTGTCATCCCCTGGATA-3'	This paper	N/A
qPCR primer: *Mus musculus Myl2* F: 5'- CGTGTTCCTCACGATGTTTG-3' R: 5'-TCAGCCTTCAGTGACCCTTT-3'	This paper	N/A
qPCR primer: *Mus musculus Myh7* F: 5'- AGCATTCTCCTGCTGTTTCC-3' R: 5'-CCAGGCCTGTAGAAGAGCTG-3'	This paper	N/A
qPCR primer: *Mus musculus Nppa* F: 5'- GGGGGTAGGATTGACAGGAT-3' R: 5'-GCAGAATCGACTGCCTTTTC-3'	This paper	N/A
qPCR primer: *Mus musculus Tnnt2 (cTnT)* F: 5'- TCAAGACCTGTGTGCAGTCC-3' R: 5'-CCACAGCTTCTTCCTGTTCC-3'	This paper	N/A

REAGENT or RESOURCE	SOURCE	IDENTIFIER
qPCR primer: *Mus musculus Tbx5* F: 5'- AGGCAGGGAGGAGAATGTTT-3' R: 5'-GCGGGAACAATATCCATGAG-3'	This paper	N/A
qPCR primer: *Mus musculus Nkx2-5* F: 5'- ACATTTTACCCGGGAGCCTA-3' R: 5'-GGCTTTGTCCAGCTCCACT-3'	This paper	N/A
qPCR primer: *Mus musculus Bra (T)* F: 5'- CCGGTGCTGAAGGTAAATGT-3' R: 5'-CCCCGTTCACATATTTCCAG-3'	This paper	N/A
qPCR primer: *Mus musculus Myh6* F: 5'- ATGTTAAGGCCAAGGTCGTG-3' R: 5'-CACCTGGTCCTCCTTTATGG-3'	This paper	N/A
qPCR primer: *Mus musculus Hand2* F: 5'- TGGCAAGGCTTTCTCCAGAC-3' R: 5'-AAGCCCTATTGCAGTGAGGG-3'	This paper	N/A
qPCR primer: *Mus musculus Sox1* F: 5'- CCCATGCACCGCTACGACAT-3' R: 5'-CGCTCATGTAGCCCTGAGAGT-3'	This paper	N/A
qPCR primer: *Mus musculus Nestin* F: 5'- GGACGCTCTCCTTCCACATC-3' R: 5'-TATCCGACCCCCACTGCTTA-3'	This paper	N/A
qPCR primer: *Mus musculus Hhip* F: 5'- CTTGTAATTGGGATGGAATGC-3' R: 5'-TCAAGGAGCCTTACTTGGACA-3'	This paper	N/A
Recombinant DNA		
Fox-enhancer-pGL4.23	This paper	N/A
Fox-enhancer-Hsp68-LacZ	This paper	N/A
Software and algorithms		
ImageJ	N/A	https://imagej.nih.gov/ij/
Seurat v4	Hao et al., 2021	https://satijalab.org/seurat/
STARsolo	Dobin et al., 2013	https://github.com/alexdobin/STAR/blob/master/docs/STARsolo.md
Scanpy	Wolf et al., 2018	https://scanpy.readthedocs.io/en/stable/
Bowtie2	Langmead and Salzberg, 2012	http://bowtie-bio.sourceforge.net/bowtie2/index.shtml
MACS2	Zhang et al., 2008	https://github.com/macs3-project/MACS
Other		
4–15% Mini-PROTEAN TGX Stain-Free Gels	Bio-rad	Cat# 17000546
Dynabeads M-280 Streptavidin	Thermo Fisher	Cat# 11205D
Dynabeads protein G	Thermo Fisher	Cat# 10003D
Ampure XP reagent	Beckman Coulter	Cat# A63880